Review

Asymmetric Coordination Environment Engineering of Atomic Catalysts for CO_2 Reduction

Xianghua Hou [1,2] , Junyang Ding [1,*], Wenxian Liu [3,*], Shusheng Zhang [4], Jun Luo [1] and Xijun Liu [2,*]

1   Center for Electron Microscopy and Tianjin Key Lab of Advanced Functional Porous Materials, Institute for New Energy Materials & Low-Carbon Technologies, School of Materials, Tianjin University of Technology, Tianjin 300384, China
2   MOE Key Laboratory of New Processing Technology for Non-Ferrous Metals and Materials, Guangxi Key Laboratory of Processing for Non-Ferrous Metals and Featured Materials, School of Resource, Environments and Materials, Nanning 530004, China
3   College of Materials Science and Engineering, Zhejiang University of Technology, Hangzhou 310014, China
4   College of Chemistry, Zhengzhou University, Zhengzhou 450001, China
*   Correspondence: junyangdingde18@163.com (J.D.); liuwx@zjut.edu.cn (W.L.); xjliu@tjut.edu.cn (X.L.)

Abstract: Single-atom catalysts (SACs) have emerged as well-known catalysts in renewable energy storage and conversion systems. Several supports have been developed for stabilizing single-atom catalytic sites, e.g., organic-, metal-, and carbonaceous matrices. Noticeably, the metal species and their local atomic coordination environments have a strong influence on the electrocatalytic capabilities of metal atom active centers. In particular, asymmetric atom electrocatalysts exhibit unique properties and an unexpected carbon dioxide reduction reaction (CO_2RR) performance different from those of traditional metal-N_4 sites. This review summarizes the recent development of asymmetric atom sites for the CO_2RR with emphasis on the coordination structure regulation strategies and their effects on CO_2RR performance. Ultimately, several scientific possibilities are proffered with the aim of further expanding and deepening the advancement of asymmetric atom electrocatalysts for the CO_2RR.

Keywords: asymmetric atom sites; coordination structure; carbon dioxide reduction reaction; catalyst design

1. Introduction

Since the first industrial revolution, the massive consumption of fossil fuels has promoted the innovation of modern science and technology and greatly raised the quality of human lifestyles [1–5]. However, the challenges of energy scarcity and atmospheric pollution are in irreversible progress, and it is imperative to formulate a clean and sustainable energy technology route [6–10]. In particular, one of the possible alternatives is to employ electrocatalytic conversions reactions to manufacture clean energy from renewable or sustainable green sources, e.g., the hydrogen evolution reaction (HER) [11,12], oxygen evolution reaction (OER) [13,14], oxygen reduction reaction (ORR) [15,16], CO_2 reduction reaction (CO_2RR) [17,18], nitrogen reduction reaction (NRR) [19,20], nitrate reduction reaction (NO_3RR), etc. [21–23]. In these proposed electrochemical reactions, the introduction of catalysts significantly reduces the extra electric energy consumption [24–28]. For traditional bulk and/or nanoparticles (NPs) electrocatalysts, only a few layers of the atoms on the surfaces of the catalysts are involved in the reactions, resulting in a large percentage of the metal atoms being ineffective and wasted. Consequently, next-generation electrocatalysts need to meet the strict demands of higher atomic utilization efficiency compared with the original ones [29–32].

In 2011, Zhang et al. prepared an atomically dispersed Pt_1/FeO_x, which was the first time the concept of a "single-atom catalyst" (SAC) had ever been applied worldwide [33]. In recent years, due to their almost 100% atomic utilization rates and exceptional activity

and selectivity, single-atom electrocatalysts have gained significant scientific attention and their development has been actively underway [34–36]. First, SACs loaded on supports not only have relatively uniform and well-defined active centers with modulated coordination bonds similar to homogeneous catalysts but also retain the advantages of easy separation, reusability, and higher stability of non-homogeneous catalysts. Thus, SACs bridge the gap between the two as a result [37–40]. Furthermore, advanced characterization strategies, as well as density functional theory (DFT) simulations, provide significant ways to comprehend the relationship between the atomic coordination environment and reaction mechanisms, which benefits from the fact that the simple electronic and coordination structures of SACs make it straightforward to identify and accurately define their functional components [41–43]. Moreover, recognizing the connection between the isolated active atomic sites and catalytic properties enables us to better define metal atom types, coordination numbers, nearby coordination dopants, geometry shapes, and electronic structures, and this can also substantially enhance the intrinsic comprehension of their activity and selectivity [44,45].

Noticeably, as shown in Figure 1, the coordination environment is as crucial as the metal center, which not only stabilizes the metal atoms but also determines the activity, selectivity, and stability of SACs. In general, the electronic structure and/or oxidation state of the metal center can be directly impacted by the first-shell atoms (direct coordination), including the type, number, and axial chemical environment of the coordination atoms, while the second- or higher-shell environment (indirect coordination) can somewhat influence the CO_2RR's performance. The classical symmetric planar four-coordination structure (MN_4: M, metal atoms; N, nitrogen atom) is one of the common structures of the active centers of carbon-based SACs for the CO_2RR. However, there are restrictions to symmetric MN_4 monoatomic sites in electrocatalytic reactions, i.e., the inappropriate adsorption strength with intermediates might result in the symmetric coordination of N atoms with high electronegativity, which causes the whole reaction process to lag. This challenge, by modifying the local coordination environment of the central metal atom, i.e., introducing the corresponding asymmetric coordination structure, can be solved to some extent. For instance, breaking the original M-N bond of MN_4 can lead to a low-coordination site MN_x ($x \leq 3$) with vacancy defects. Alternatively, by introducing heteroatoms to replace some of the coordination N atoms of MN_4, it becomes possible to construct MN_xY with heteroatomic coordination structure sites (Y is other coordination atoms such as O, S, Cl, F, etc.), and the heteroatoms can also replace atoms on different coordination shells around the metal center. In addition, when two isolated MN_4 sites are close enough, they can transform into neighboring metal atom sites $M_1M_2N_x$. These asymmetric atomic sites, by adjusting the electronic structure of the catalyst to break the inappropriate adsorption strength between the atomic active sites and the reaction intermediates, optimize the adsorption-desorption process of reactants and products and further improve the electrocatalytic performance, demonstrating how the local coordination environment has a significant impact on the energy barriers and reaction paths [46–50].

So far, many impressive review papers have summarized the synthesis, characterization, and catalytic performance of SACs [51–53]. However, methods for breaking the symmetry of metal-N_4 sites, and the unique electronic structure and CO_2RR catalytic behavior of asymmetric atom sites, are rarely summarized [54,55]. In this review, we introduce the influence of the asymmetric coordination structure on the intrinsic electrochemical activity of SACs for the CO_2RR, including low coordination, heteroatom coordination, dual-metal sites, and the second coordination shell. In addition, the synthesis strategy of asymmetric SACs, and the structure-function relationship between coordination structure and CO_2RR performance are highlighted (Figure 1). Finally, the challenges, opportunities, and future development directions of SACs for electrocatalytic energy conversion technology are discussed.
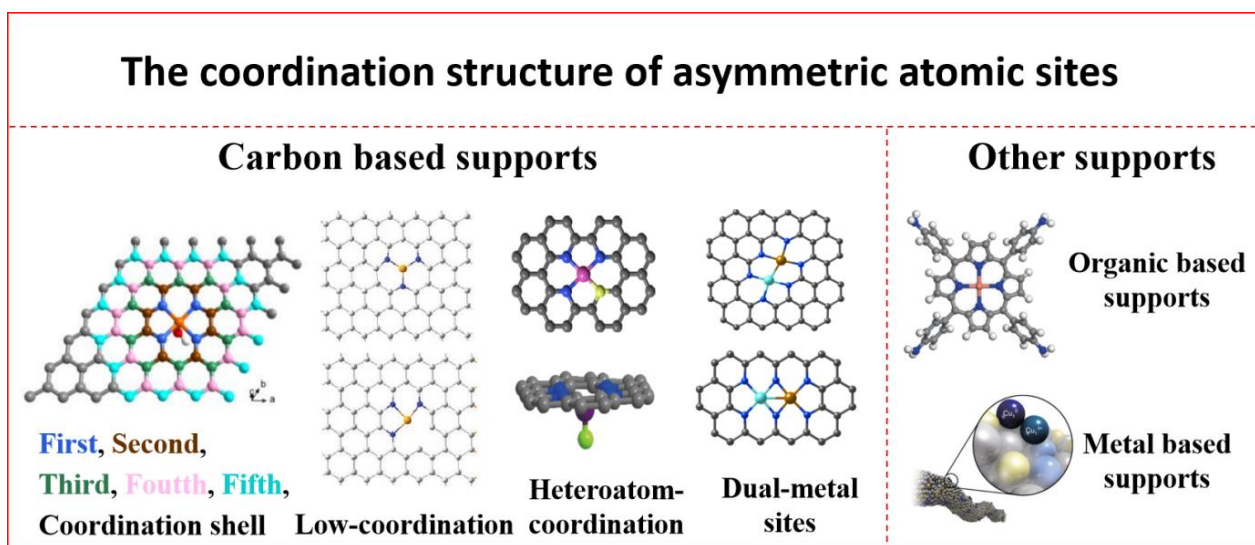
The coordination structure of asymmetric atomic sites

Carbon based supports

First, Second,
Third, Foutth, Fifth,
Coordination shell   Low-coordination   Heteroatom-coordination   Dual-metal sites

Other supports

Organic based supports

Metal based supports

Figure 1. Model diagrams of symmetric and asymmetric atomic configurations. (The heteroatom coordination (bottom) elements are reprinted with permission from ref. [56], copyright: (2019) Nature Publishing Group; the organic-based support elements are reprinted with permission from ref. [57], copyright: (2021) Nature Publishing Group; other elements are taken from Figures 2–7.)

2. Advantages of Asymmetrically Coordinated SACs

Initially, in 2015, Varela et al. reported that the carbon-based catalysts (Fe/Mn-N-C) with doped N and Fe/Mn species demonstrated a higher CO selectivity of up to 80% at -0.5 V vs. RHE, which is superior to polycrystalline Au electrodes [58] and other comparable metal-N-C materials (e.g., the Co protoporphyrin, Ni^{2+} on N-doped graphene, Rh-porphyrin-like functionalized graphene, etc.) [59–61]. Then, the researchers identified that FeN_4 moieties were the primary active sites for the selective CO_2 reduction into CO with up to 80% FE_{CO} in an aqueous solution (Figure 2a,c) [62], whereas Fe nanoparticles (NPs) mostly catalyzed hydrogen evolution [63]. Through using DFT calculations, the CO_2RR mechanism of Fe-N_4-embedded N-doped graphene was further investigated, finding that the CO_2 molecules preferred to adsorb on the Fe catalytic site, while the neighboring N atoms promoted the formation of COOH* and the release of CO*, thus improving the conversion efficiency (Figure 2b) [62].
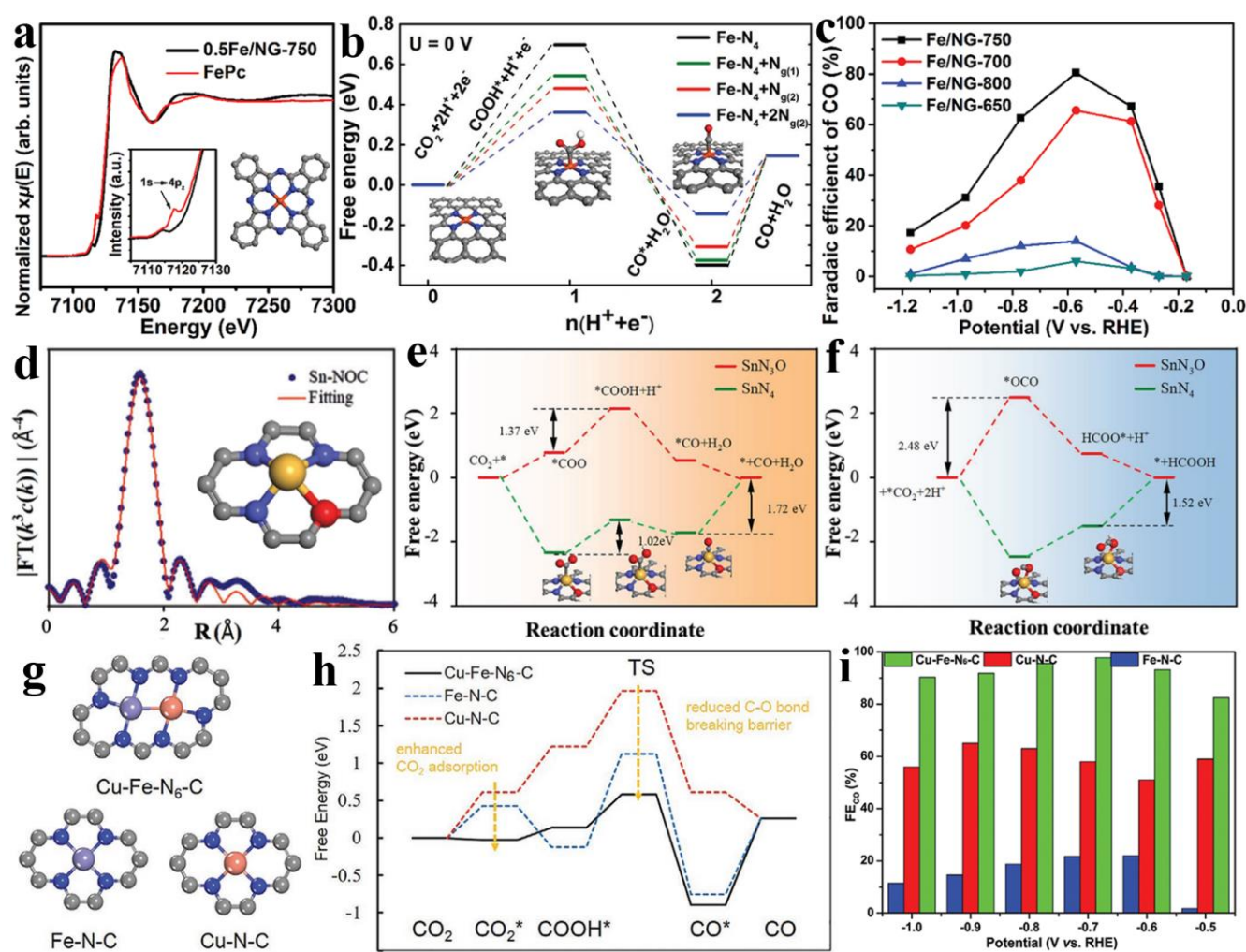
Figure 2. (**a**) Normalized Fe K-edge X-ray adsorption near-edge structure (XANES) spectra of 0.5Fe/NG-750 catalyst. (**b**) Free energy diagram for electrochemical CO_2 reduction to CO. (**c**) CO Faradaic efficiency (FE_{CO}). Reprinted with permission from ref. [62]. Copyright: (2018) WILEY-VCH Verlag GmbH & Co. KGaA, Weinheim. (**d**) The Fourier transform extended X-ray absorption fine structure (FT-EXAFS) fitting curve for Sn-NOC in R space. The calculated Gibbs free energy diagrams for (**e**) CO_2-to-CO conversion and for (**f**) CO_2-to-HCOOH conversion. Reprinted with permission from ref. [64]. Copyright: (2021) The Authors. Advanced Science published by Wiley-VCH GmbH. (**g**) Atomic models of Cu-Fe-N_6, Fe-N_4, and Cu-N_4 catalytic centers. (**h**) Free energy profiles for CO_2 electroreduction reactions. (**i**) FE_{CO} of Fe-N-C, Cu-N-C, and Cu-Fe-N_6-C. Reprinted with permission from ref. [65]. Copyright: (2020) Wiley-VCH GmbH.

Furthermore, in a work on a N-doped porous carbon matrix including isolated FeN_x moieties with different N coordination numbers, it was revealed that when compared with perfect FeN_4 and the Fe-N_3 atomic site, the low-coordinated FeN_3V active center effectively reduced the free energy barrier for promoting the formation of intermediates *COOH of rate determination step, so that Fe_1NC/S_1-1000 with Fe-N_3V atomic sites demonstrated a high 96% FE_{CO} [66]. In addition to controlling the N coordination number, heteroatoms exist in different coordination shell locations or spatial orientations to alter the catalytic activity of the atomic metal center. For instance, in contrast with the traditional Sn-N_4 configuration, which mostly produces HCOOH and H_2 products, N-rich carbon catalysts made up of atomically dispersed SnN_3O_1 active sites have CO as the main product (Figure 2d). According to DFT calculations, SnN_3O_1's atomic configuration lowers the activation energy barrier for *COO and *COOH generation ($\triangle G$ = 1.37 eV) while significantly raising the energy barrier for the production of *OCO ($\triangle G$ = 2.48 eV), which encourages the conversion of CO_2

to CO and inhibits the production of HCOOH, opening up a new route for the selectivity of particular products (Figure 2e,f) [64]. Single atoms can also form metal-metal bonds with other metals in order to build binary atom sites with the unique advantage of synergistic effects. The resulting Fe/Cu-N-C catalysts exhibited excellent >95% FE_{CO} with a wide potential range from -0.4 to -1.1 V vs. RHE (Figure 2g,i), which was primarily attributed to the bifunctional active sites, i.e., the Cu site has a greater affinity for molecular CO_2 (CO_2 adsorption energy: Cu-Fe-N_6-C, -0.03 eV; Fe-N-C, 0.43 eV; Cu-N-C, 0.61 eV), increasing the CO_2 concentration, while the Fe site inhibits hydrogen evolution (Figure 2h) [65,67]. In conclusion, through the modification of the MN_4 coordination environment, including the metal center, the coordination atom numbers, the coordination atom species, and the position or spatial orientation of the coordination shell had a significant influence on the microscopic properties and catalytic activity of the SACs. Based on a more detailed comparative evaluation, owing to the high electronegative N components in the local structure, the symmetric MN_4 moiety may lead to an inappropriate adsorption strength with the intermediate and can slow down the entire reaction process, causing problems such as low product selectivity and a high reaction overpotential. Meanwhile, the active site's electronic and geometric asymmetry can control the adsorption-desorption behavior of the crucial reaction intermediates, which is beneficial in lowering the reaction energy barrier, preventing the occurrence of side reactions, and accelerating the reaction rate, all of which contribute to improved catalytic activity.

3. The Synthesis Strategies for Breaking MN_4

There are two main routes to breaking the M-N bond of MN_4. One is the carbonization of precursors such as metal-organic frameworks (MOFs) and polymers with nitrogen-containing specie ligands or other mixtures containing metal salt and nitrogen sources (such as urea, melamine, dicyandiamide, N_2, NH_3, etc.), in which the coordination number can be controlled by finely modulating temperature [68]. Another is the pre-construction of N-doped graphene with abundant defects, vacancies, or edges, and subsequently introducing metal sources that are immobilized in the pre-existing positions of graphene via pyrolytic dispersion to produce low-coordinated metal atoms [69,70]. For instance, the weaker M-O bond is broken in the M-N_xO_y hybrid coordination structure, followed by the removal of the oxygen atom, producing an atomically scattered M-N_x catalyst [71]. In addition, M-N bonds can also be broken by using sophisticated plasma treatments [72,73].

The introduction of coordinated heteroatoms beyond N can be achieved via the following methods: (i) pre-storing in the precursor through coordination, impregnation, encapsulation, grinding, or other physical mixing styles; (ii) using biomass precursors or polymers rich in a variety of non-metallic elements (purslane, chitosan, cyanobacteria, etc.); (iii) for materials with low boiling points, such as S, P, and I, one can diffuse onto the carbon substrate via the sublimation effect during carbonization, coordinating with metals, or replacing carbon atoms; and (iv) using reactants that contain certain heteroatoms, such as S powder, thiourea, and sulfur salts for S, triphenylphosphine, NaH_2PO_2, and polypyrrole for P, NH_4I and I_2 for I, HCl, NaCl, and KCl for Cl, borane and boronic acid for B, and polytetrafluoroethylene for F [74–83].

The construction of homonuclear/heteronuclear bimetallic atoms is commonly achieved via increasing the concentration or species of the metal salts, usually accompanied by monometallic sites. For the fabrication of homonuclear sites, the increased metal amount means raising the possibility of NPs [84]. Ligand-protected diatomic nodes can be designed using MOF substrates acting as metal precursors [85]. Recently, an anion replacement deposition-precipitation method was reported, in which water-soluble M_2 precursors become insoluble after anion replacement and were thus deposited onto a pre-prepared carrier [86]. For heteronuclear sites, one method is to encapsulate two metal salts into the pore channels of the MOF template [87], and another is to prepare a mixed precursor containing a nitrogen source, carbon source, and double metallic source [88]. Preparing high-quality bimetallic structures using atomic layer deposition (ALD) technologies, where

the second metal can only be attached to the primary metal by modulating the deposition conditions, has also been demonstrated to be effective [89].

4. The Characterization of Asymmetric Atom Sites

Currently, there are two main characterization tools for describing single atomic sites: high-angle annular dark-field scanning transmission electron microscopy (HAADF-STEM) and XAFS.

The resolution of HADDF-STEM images can reach up to 1 Å, allowing a fine distinction between individual atoms [90]. For instance, Zhang et al. reported a conception in which graphene defects capture Ni single atoms as active sites, as shown in Figure 3a, and identified the presence of di-vacancy defects that trap an atomic Ni species (aNi@Di-vacancy) [91]. Furthermore, Liu et al. synthesized an atomic dispersed cobalt-based catalyst with a doped I species that has low-coordination CoN_3 and IN_3 sites (Co-I-N/G). Through atomic-scale HAADF-STEM images (Figure 3b) and a Z-contrast analysis, two sets of uniformly distributed bright spots with different intensities (marked by green and yellow circles, respectively) were attributed to Co and I atoms, respectively [92]. For dual-atom sites, Zhou et al. presented a bimetallic (Rh-Fe) interbond as an ideal chemical facilitator (FR-NCS) that can facilitate the dispersion of Fe atoms. In Figure 3c, most of the Fe and Rh are uniformly and atomically dispersed on the nitrogen-doped carbon hollow spheres shell (highlighted by blue circles), and Fe-Rh "hetero-pair" atoms are found in Figure 3d, demonstrating the formation of an Rh-Fe interband [93]. In short, it can be noted that the STEM technique does not acquire accurate structural information about the atom species and coordination number.

EXAFS can be used to calibrate the atomic species and obtain the neighboring atom structure, and, thus, is an indispensable tool for investigating asymmetric coordination [94]. Sui et al. synthesized an effective CO_2RR catalyst featuring Ag atoms coordinated with three nitrogen atoms (Ag_1-N_3, Figure 3e). In the EXAFS spectra, a significant peak in the Ag-SACs' EXAFS spectra at 1.5 Å is attributed to Ag-N scattering, but there is no Ag-Ag scattering at 2.6 Å, indicating an atomically dispersed Ag species (Figure 3f). In the EXAFS fitting curves (Figure 3g,h), the Ag-N coordination numbers of Ag_1-N_3/PCNC and Ag_1-N_2/PCNC are fitted from 3.1 to 1.9, respectively, demonstrating the formation of Ag_1-N_3 and Ag_1-N_2 coordination structures. The electrochemical test results showed the trend of the CO Faradaic efficiency (FE_{CO}) sequence, Ag_1-N_3/PCNC > Ag_1-N_2/PCNC > Ag NPs/C > CFP, confirming that Ag_1-N_3 was the best active site among them (Figure 3i) [95].
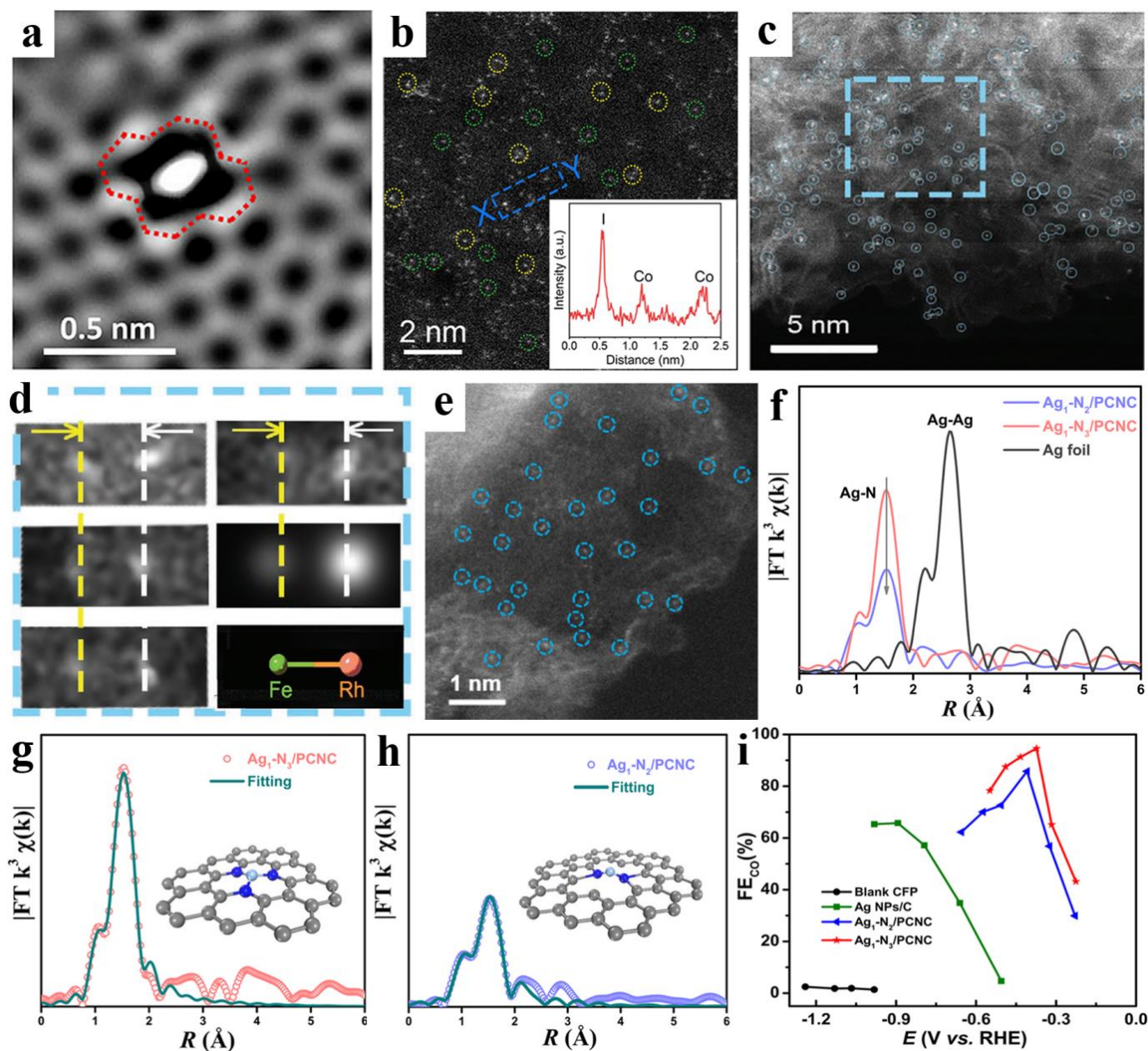
Figure 3. (**a**) HAADF-STEM image of the defective area with atomic trapped Ni. Reprinted with permission from ref. [91]. Copyright: (2017) Elsevier Inc. (**b**) Atomic-scale HAADF-STEM image of Co-I-N/G. Reprinted with permission from ref. [92]. Copyright: (2021) American Chemical Society. (**c**) HAADF-STEM image of FR-NCS. (**d**) The zoomed-out blue rectangular area showing the existence of adjacent dual-metal atoms. Reprinted with permission from ref. [93]. Copyright: (2020) Wiley-VCH GmbH. (**e**) Aberration-corrected STEM images of Ag_1-N_3/PCNC. (**f**) EXAFS spectra. (**g**,**h**) EXAFS fitting curves at R space. (**i**) FE_{CO}. Reprinted with permission from ref. [95]. Copyright: (2021) American Chemical Society.

5. Asymmetric Atom Sites for CO_2RR

5.1. Low-Coordination Structure

Eliminating part of the coordinated N atoms from the original symmetric MN_4 results in the corresponding defective sites, i.e., the low-coordinated MN_x configuration. The low-coordination sites of MN_x (M = Fe, Co, Ni, Cu, Zn, Mn, Ag, etc.; x < 4) are mainly constructed in two strategies: one is a one-step method to obtain the desired coordination numbers, and the other is breaking the original metal-coordination bond.

In abundant atomically dispersed based metal-nitrogen co-decorated carbon (M-NC) materials, some transition metals, i.e., Fe, Co, Ni, and Cu, can facilitate charge transfer to account for their unfilled 3d orbitals. Wang et al. reported the gas diffusion of ferrocene and thermal activation (800–1000 °C) to successfully fabricate isolated Fe atoms loaded on N-doped porous carbon polyhedrons (Figure 4a) with different N coordination numbers (FeN_4, FeN_3). According to DFT calculations and experimental measurements, the Fe-N_3V active centers have most balanced free energy barriers of intermediates, CO_2 to *COOH (0.47 eV), *COOH to *CO (0.15 eV), and *CO to CO (0.14 eV), strengthening its CO_2RR performance. At the same applied potential of -0.5 V vs. RHE, the FE_{CO} of Fe_1NC/S_1-1000, Fe_1NC/S_1-900, and Fe_1NC/S_1-800 are 96%, 90%, and 82%, respectively (Figure 4b,c) [66]. Similarly, three atomically dispersed Co catalysts (800 °C, Co-N_4; 900 °C, Co-N_3; and 1000 °C, Co-N_2) can be selectively synthesized by adopting various pyrolysis temperatures of bimetallic Co/Zn ZIFs. The Co-N_2 could acquire a better selectivity and activity compared with other Co-N_x, which demonstrated that the inert reactive sites could also be activated by adjusting the coordination environment (Figure 4d,e) [96]. Rong et al. adopted the other strategy that differs from those mentioned above to construct a vacancy-defect Ni site. The single-atom Ni-N_3O mixed-coordination precursors were first synthesized at 500 °C and then heated to 800 °C, where the oxygen atoms could be subsequently eliminated on account of the weaker Ni-O interactions, leading to atomically dispersed Ni-N_3-V catalysts (Figure 4f). It was discovered that the electrocatalytic activity of the CO_2RR can be significantly enhanced after the introduction of vacancy defects in Ni-N_3-V SACs, compared with the difficulty of the NiN_3 site to release CO ($\triangle G$ = 1.264 eV), and this is mainly attributed to Ni-N_3-V's optimized and moderate CO_2 to COOH* reaction free energy ($\triangle G$ = 0.680 eV) (Figure 4g) [71]. Calculations further disclose that the active site is the particular defect-Ni-N_3 structure [97]. Moreover, the Ni-pyridinic N_2V_2 is quickly generated as a result of the high-energy plasma's constant collision and presents a more advantageous comprehensive performance than other Ni-pyridinic N_xC_{3-x} species, resulting in a higher CO_2RR efficiency and worse HER activity (Figure 4h,i) [72]. Lin et al. found that the FE_{CO} of both the NiN_2 site and FeN_4 site is proportional to the reaction temperature, but that the NiN_2 site is more effective, which stems from the variation in the adsorption strength of the key intermediates between the two [98]. Cu-based nanocatalysts are frequently utilized for the construction of a wide range of C_{1+} and C_{2+} products [99]. The work of Guan et al. showed the significance of the distance between isolated atomic copper sites for the electroreduction of CO_2 to various hydrocarbons (Figure 4j). DFT calculations indicate that high 4.9%$_{mol}$ Cu concentrations with adjacent Cu-N_2 sites are more advantageous for the formation of C_2H_4 due to the reduced free energy of the C-C coupling, while all isolated Cu-N_4, neighboring Cu-N_4, and isolated Cu-N_2 sites tend to generate C_1 products when the concentration of Cu is less than 2.4%$_{mol}$ [100].

To date, Zn-NC has received less attention compared with other transition metals (Fe, Co, Ni, and Cu), and it is generally believed that when the $3d^{10}$ orbital is fully occupied, it can significantly impair electron transport and lower the electrocatalytic activity of Zn. Li et al. reported a N-anchored low-valence Zn single-atom catalyst that contains saturated four-coordinate (ZnN_4) and unsaturated (Zn-N_3) active sites. The unsaturated Zn-N_3 could dramatically reduce the energy barrier by stabilizing the COOH* intermediate, thus allowing simultaneous large current densities of up to 1 A cm^{-2} and high CO selectivity of up to 95% using flow cell devices (Figure 4k) [68]. Compared with the poor selectivity and activity (65% FE_{CO}, 3.3 mA cm^{-2} of j_{CO}) of Mn-N_4 [58], the Mn-N_3 center in Mn-C_3N_4/CNT can attain an excellent CO_2RR performance (98.8% FE_{CO}, 14.0 mA cm^{-2} of j_{CO}). In situ X-ray absorption spectra and DFT calculations reveal that the Mn-N_3 site can lower the free energy barrier for the production of the crucial intermediate COOH*, which is responsible for high catalytic performance (Figure 4l) [101]. Additionally, altering the coordinate environment of the Ag atoms can boost their activity. It was shown that the Ag_1-N_3 site performed better than Ag_1-N_2 and Ag NPs, owing to its lower CO binding energy [95].
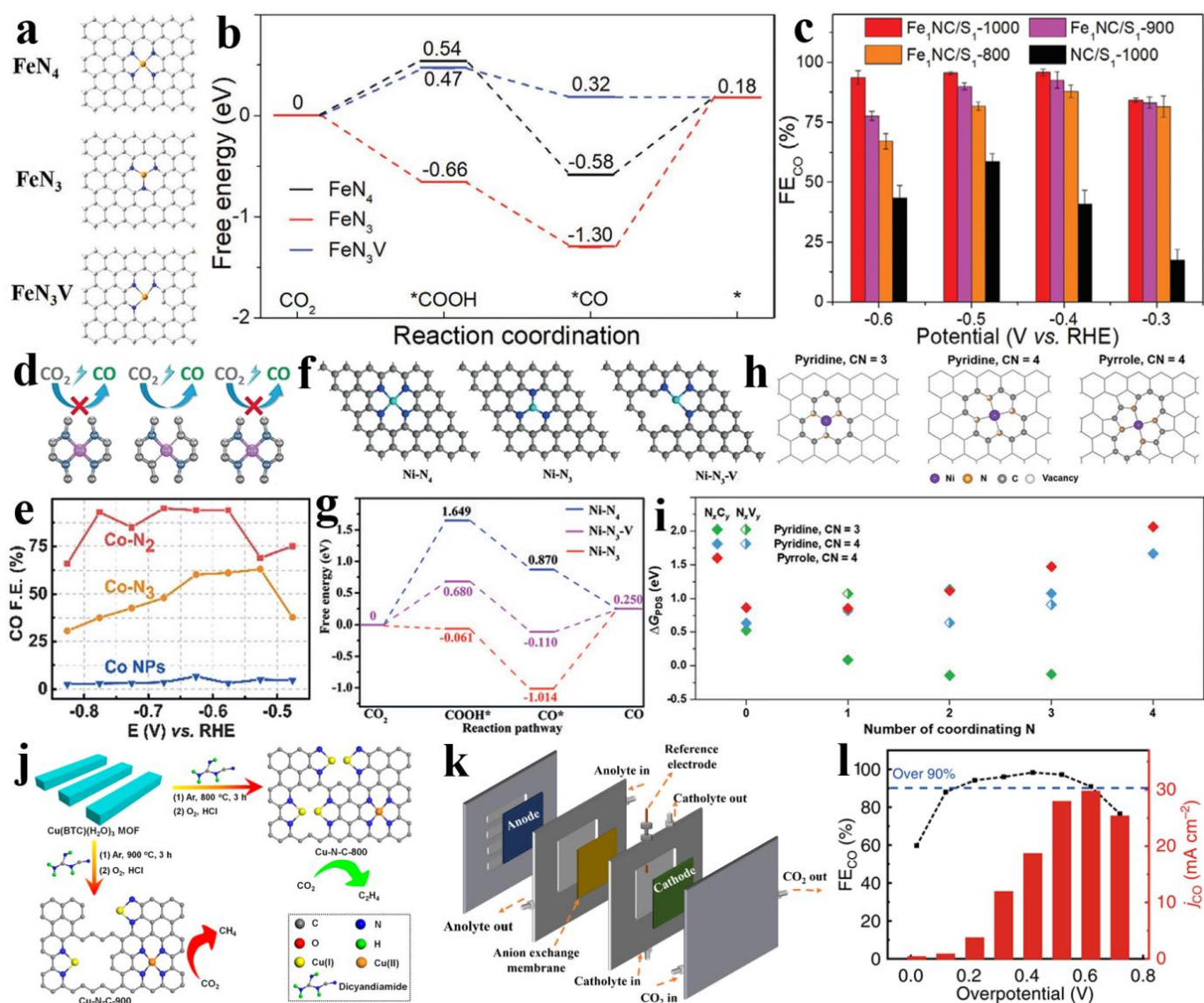
Figure 4. (**a**) The optimized atomic structures of FeN_4, FeN_3, and FeN_3V. (**b**) The calculated free-energy diagrams. (**c**) FE_{CO}. Reprinted with permission from ref. [66]. Copyright: (2020) WILEY-VCH Verlag GmbH & Co. KGaA, Weinheim. (**d**) Atomic structures of CoN_4 and CoN_2 on graphene. (**e**) FE_{CO}. Reprinted with permission from ref. [96]. Copyright: (2018) Wiley-VCH Verlag GmbH & Co. KGaA, Weinheim. (**f**) The optimized atomic structures of Ni SACs. (**g**) Calculated free-energy diagram. Reprinted with permission from ref. [71]. Copyright: (2020) Wiley-VCH Verlag GmbH & Co. KGaA, Weinheim. (**h**) Different coordination structures of NiNG SACs. (**i**) The calculated free energy change at potential determining step (PDS; ΔG_{PDS}). Reprinted with permission from ref. [72]. Copyright: (2021) Wiley-VCH GmbH. (**j**) Schematic of preparation of the Cu-N-C-T catalysts. Reprinted with permission from ref. [100]. Copyright: (2020) American Chemical Society. (**k**) Schematic of flow-cell configuration. Reprinted with permission from ref. [68]. Copyright: (2021) Wiley-VCH GmbH. (**l**) FE_{CO} and current density of CO (j_{CO}) of Mn-C_3N_4/CNT in the CO_2-saturated [Bmim]BF_4/CH_3CN-H_2O electrolyte. Reprinted with permission from ref. [101]. Copyright: (2020) Nature Publishing Group.

The investigation of the above works reveals that the reduced oxidation state of the monoatomic metal center with low coordination numbers makes it easier to adsorb reactant molecules, and optimize the adsorption strength of intermediates, especially COOH* in the CO product process. In addition, we also speculate that the extra space caused by

low coordination also facilitates a more flexible matching between reactant molecules and active sites.

5.2. Lateral Heteroatom Coordination Structure

The doping of non-metallic atoms in carbon supports is an efficient and flexible technique for improving the overall performance of SACs, such as through the introduction of heteroatoms to replace the coordinated N atoms in the symmetrical planar MN_4 sites to form a lateral heteroatom coordination structure. The laterally coordinated non-metallic heteroatoms, such as C, N, S, O, B, P, F, etc., could modulate the coordination environment of the atomic metal active center through direct coordination (first coordination shell) and indirect coordination (second or higher coordination shell), thereby achieving the goal of optimizing the reaction path.

In 2017, Zhao et al. reported ZIF-8-derived NiN_3C_1 single atomic catalysts for the efficient electroreduction of CO_2. The positive correlation between HCO^{3-} concentration and the efficiency of CO_2 electroreduction was disclosed (Figure 5a), which mainly benefits from the dual roles of HCO^{3-} (the proton donor in the reaction solution, the ideal equilibrium carrier for CO_2) [102]. Gong et al. used non-nitrogenous MOFs, bimetallic MgNi-MOF-74 with extra pyrrole (Py) N sources, to construct a series of NiSA-N_x-C (x = 2, 3, 4) at various carbonation temperatures (Figure 5b), wherein the NiSA-N_2-C could easily facilitate the formation of the COOH* intermediate and therefore result in its remarkable activity (Figure 5c) [103]. Yang et al. also observed that the N coordination number dropped from 4 to 1, while the C coordination number grew throughout the construction process of the Ni@N_xC_y catalysts when the temperature was raised from 800 to 1100 °C [104]. Of note is the charge capacity of the site for facilitating the electrochemical steps as well as hydrogen bonding to the intermediate for stabilizing the intermediates, which were often ignored in previous DFT calculations and are indispensable [105]. To lower the production investment of single-atom catalysts, Zu et al. synthesized kilogram-scale $Sn^{\delta+}$ on N-doped graphene (SnN_2C_2) using a rapid freeze-vacuum drying-calcination procedure, and its electroreduction activity basically remained inactive even after 200 h (Figure 5d) [106]. Sulfur and oxygen atoms have been viewed as ideal alternatives for coordinated N in the metal-Nx center because of their lower electronegativity than N, having the ability to dramatically change the active center's local electronic densities [107]. Wang et al. developed an atomically dispersed N, S co-coordinated Bi site catalyst (Bi-N_3S/C) shown in Figure 5e, which achieved up to 98.3% FE_{CO} at −0.8 V vs. RHE, which is significantly better than Bi-SAs-N/C, and this demonstrated that the introduction of S can greatly lower the energy barrier of the intermediates of the rate-determining step [108]. Sometimes, other strategies are employed in cooperation with heteroatomic coordination to increase a catalyst's activity. In a S/N dual-heteroatom anchored unsaturated Ni site (NiN₂S-V), the decreased energy barriers for the electroreduction of CO_2 to CO are a result of both doped S atoms and evolved S vacancies [109]. As shown in Figure 5f, this synergistic interaction was also verified by Chen et al. via developing a tandem catalyst consisting of a single Cu site with N and S co-coordinated and atomically dispersed Cu clusters (Cu-S_1N_3/Cu_x) [110]. Guo et al. demonstrated the difference between prepared SnN_3O_1 (CO product) and a classic SnN_4 (HCOOH product) configuration for CO_2-to-CO conversion [64]. Meanwhile, Sn-C_2O_2F catalysts with distinctive non-nitrogen coordination structures also support the opinion just mentioned according to the selectivity of CO_2RR products [83]. In addition, the smaller radii of the electron-deficient B make it vulnerable to coordinate with the electron-rich N via electron-sharing effects, such as with the B-doping in B/N co-coordinated atomic Fe-based catalyst (Fe-N_3B) that also facilitated *COOH formation and inhibited hydrogen generation [82]. Indirectly coordinated heteroatoms (secondary or higher coordination shells) can also induce local electric fields and change the catalytic behavior of the catalytic center. Chen et al. reported S doping in the second coordination shell of FeN_4 (FeN_4S), shown in Figure 5g, and Gu et al. finished the B bridging atomic coordination of NiN_4 (NiN_4B_2) shown in Figure 5h, both inducing an enhanced CO_2RR performance relative to

pristine FeN_4 as well as NiN_4, respectively [111,112]. P, in the N group, as a classic electron donor, through integrating into carbon substrates, can alter the electronic structure of the metal site via its 3p lone pair electrons. In Sun et al.'s work on Fe-SAC/NPC (FeN_4O_1-P), by fitting FT-EXAFS spectra in R space, each Fe atom was separated by four Ns and one O, while a single P in high-coordination shells ($n \geq 3$) was merged mainly as P-C bonds into the N-doped carbon (Figure 5i), and the P of the third coordination shell enhanced the stability of the key *COOH intermediate on Fe, resulting in an outstanding CO_2RR performance at a low applied potential [113].
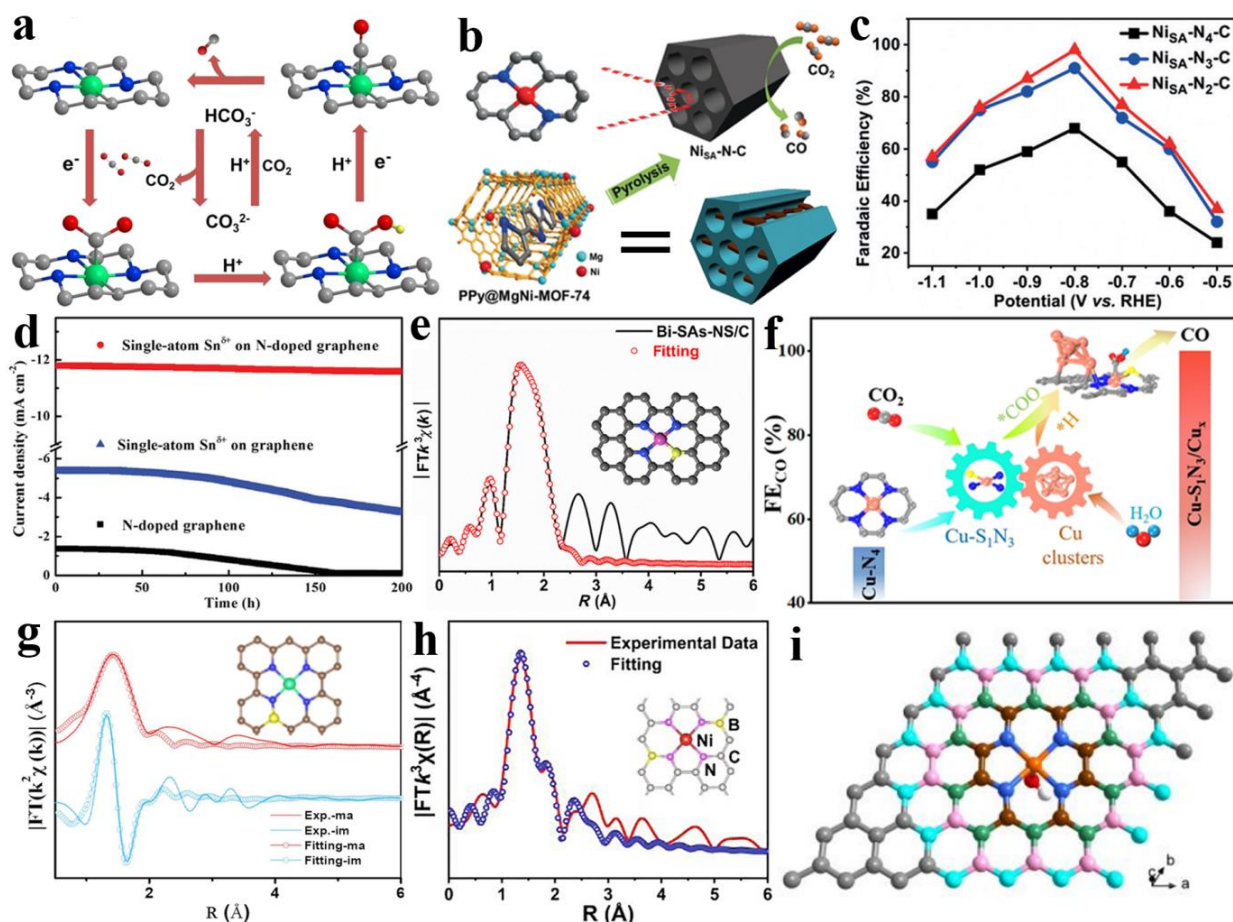

Figure 5. (**a**) Proposed reaction paths of Ni SAs/N-C for CO_2RR. Reprinted with permission from ref. [102]. Copyright: (2017) American Chemical Society. (**b**) Schematic of preparation of the NiSA-N_x-C catalysts. (**c**) FE_{CO}. Reprinted with permission from ref. [103]. Copyright: (2019) Wiley-VCH Verlag GmbH & Co. KGaA, Weinheim. (**d**) Chronoamperometry test of single-atom $Sn^{\delta+}$ on N-doped graphene at the potentials of -1.6 V versus SCE. Reprinted with permission from ref. [106]. Copyright: (2019) WILEY-VCH Verlag GmbH & Co. KGaA, Weinheim. (**e**) The EXAFS fitting for Bi-SAs-NS/C. Reprinted with permission from ref. [108]. Copyright: (2021) Tsinghua University Press and Springer-Verlag GmbH Germany, part of Springer Nature. (**f**) Schematic of Cu-S_1N_3/Cu for CO_2RR. Reprinted with permission from ref. [110]. Copyright: (2021) Wiley-VCH GmbH. (**g**) The fitting EXAFS spectra of Fe_1-NSC and fitting model. Reprinted with permission from ref. [111]. Copyright: (2022) Wiley-VCH GmbH. (**h**) The FT-EXAFS spectrum for Ni-SAs@BNC. Reprinted with permission from ref. [112]. Copyright: (2022) Elsevier Ltd. (**i**) Different local structures of FeN_4O-graphene: the second (wine, FeN_4OP_2), third (olive, FeN_4OCP_3), fourth (pink, FeN_4OCP_4), and fifth (cyan, FeN_4OCP_5) coordination shell of Fe center. Reprinted with permission from ref. [113]. Copyright: (2021) Wiley-VCH GmbH.

In short, heteroatom coordination has a greater influence on CO_2RR conversion compared with lower coordination strategies and can even completely change the obtained

product, e.g., SnN_4, a classical formic-acid-producing catalyst, transforms into CO after the introduction of a coordinated O or F. Further enhancement of the understanding of the mechanism of heteroatom action can expand the choice of products.

5.3. Axial Heteroatom Coordination Structure

Heteroatoms in the conductive carbon supports can function as bridges to axially couple to MN_4 sites, while isolated heteroatoms can also build axial coordination patterns in the form of unsaturated coordination (dangling atoms). The various heteroatoms can directly coordinate with the single atomic M center in the symmetric MN_4 to construct an asymmetric axial coordination structure of MN_4X_1 (X = N, O, S, Cl, F), which is essentially identical to the function of the lateral structural configuration, i.e., to obtain a more suitable electron structure and performance than pristine MN_4.

Zhang et al. designed a graphene-confined atomic dispersed FeN_5 catalytic site in Figure 6a–c, in which the electron density of the Fe 3d orbitals is further consumed through axial pyrrolic N, thus weakening the Fe-CO π back donation, resulting in a fast desorption toward CO and high selectivity (only at -0.46V vs. RHE, up to ~5 mA cm^{-2}, FE_{CO} ca. 97.0%) [114]. After the substitution of axial N by O, the corresponding catalytic activity of the obtained $Fe_1N_4O_1$ was further strengthened (-0.56 V to -0.87 V vs. RHE, up to ~15 mA cm^{-2}, FE_{CO} nearly 100%), as shown in Figure 6d–f [115]. Simultaneously, similar satisfactory results were also achieved for NiN_4O (-0.5 V to -1.1V vs. RHE, up to ~30 mA cm^{-2}, FE_{CO} above 90%), which could be responsible for the axial traction effect with an additional axial oxygen atom in Figure 6g–i [116]. Additionally, the one-pot template sacrificial pyrolysis method used by Huang et al. promises the development of a series of metal-N_4-O catalysts, such as well-defined Ni-N_4-O, for a variety of catalytic applications [117]. Aiming to attain the targets of high selectivity, high current density, and long-term stability, Wu et al. designed and prepared a CdN_4S_1/CN catalyst that is effective for the electrochemical reduction of CO_2 to CO (-2.1 V to -2.7 V vs. Ag/Ag$^+$, FE_{CO} more than 95%) in H-type cells with [Bmim]PF$_6$-MeCN cathodic electrolytes and also reaches an outstanding current density of 182.2 mA cm^{-2}, which is majorly owing to the reason that Cd can inhibit HER as well as S with a high spin density and charge delocalization can lower the key free energy barrier. Thus, the CdN_4S_1 site has a lower free energy barrier for the CO_2RR (0.27 eV) and higher free energy barriers for the formation of H* for the HER (0.49 eV) (Figure 6j–l) [118]. Furthermore, Huang et al. designed a new Ni-N_5-C single-atom catalyst with an enzyme-like catalytic active site and then evaluated its performance using a flow cell device, achieving a maximum current density of 1.23 A cm^{-2} at -2.4 V vs. RHE with a 99.6% FE_{CO} and 100 h continuous stable operation [119]. In addition, in some reported works, Cl and F are also used as axial coordination atoms of MN_4 to improve the electroreduction properties of CO_2, such as FeN_4Cl/NC and MnN_4Cl, and, although both of them can achieve a high selectivity of >90%, they are limited to a narrow lower potential window [56,78]. In another specialized configuration catalyst of SnC_2O_2F, the F atom bonded to Sn has a significant capability to inhibit hydrogen evolution [83].

By summarizing the above-mentioned works, it can be found that the activity of the CO_2RR is gradually enhanced by modifying the axial coordination atoms or optimizing the choice of metal centers, and the axial coordination atoms seem to be more advantageous in inhibiting hydrogen precipitation. Importantly, the choice of electrolyte, such as ionic liquids, also has a significant effect on the improvement of CO_2RR yield.

5.4. Dual-Metal Coordination Structure

Bimetallic atomic sites, i.e., neighboring monoatomic sites, provide more opportunities for the manipulation of the electrical and geometric structures of SACs on the basis of preserving atomic dispersion. Differing from SACs, bimetallic heteroatomic site catalysts, mainly including M_1N_4-M_2N_4, $M_1M_1N_x$, $M_1M_2N_x$, etc., utilize two adjacent metal atoms to achieve a functional association and synergistic effect and, furthermore, through the elec-

tronic interactions between them, to efficiently tailor the binding strength of intermediates as well as optimize CO_2RR activity.
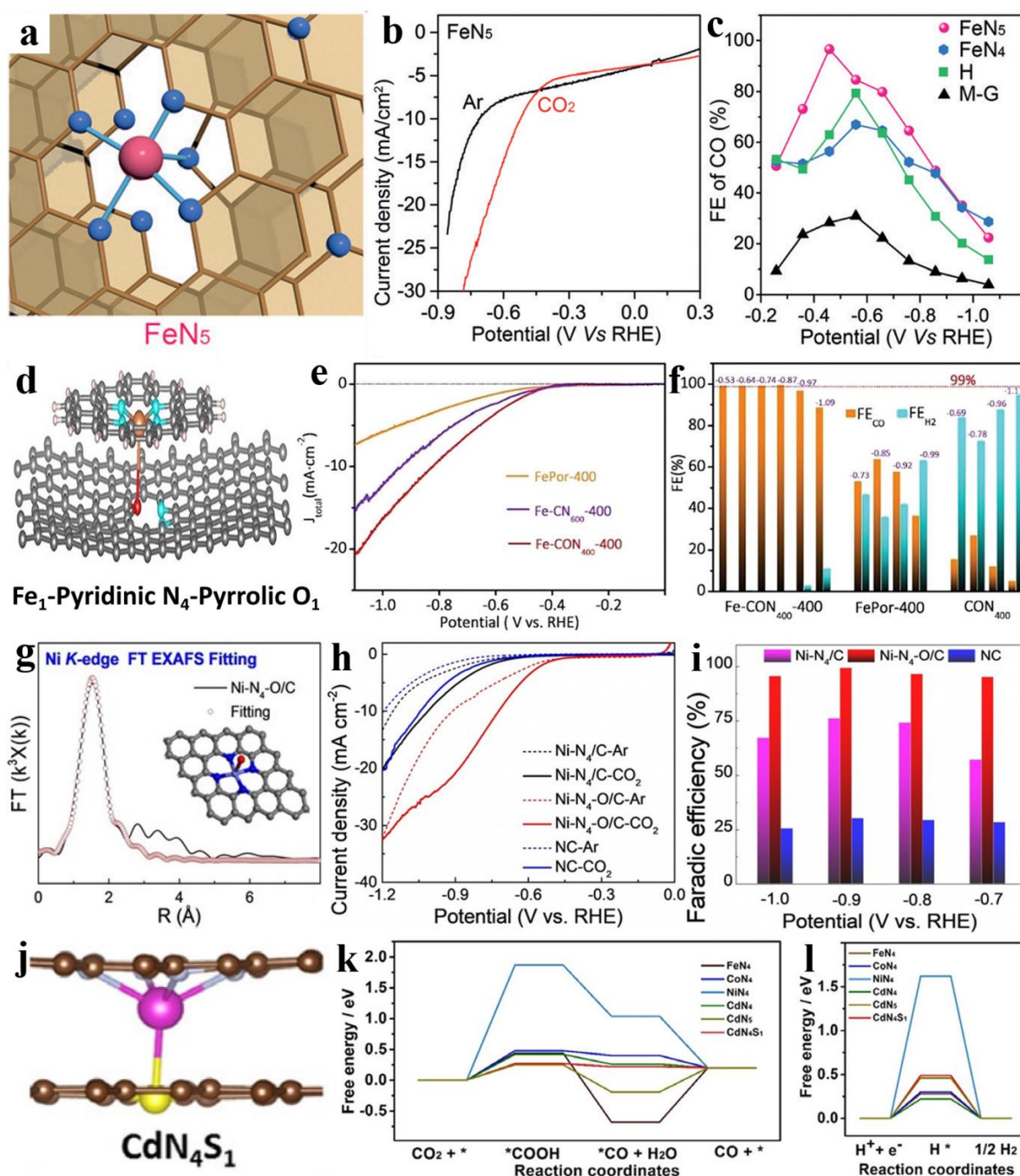

Figure 6. (**a**) The local structure of FeN_5 catalysts. (**b**) The linear sweep voltammetric (LSV) curves in 0.1 M $KHCO_3$ solution. (**c**) FE_{CO}. Reprinted with permission from ref. [114]. Copyright: (2019) Wiley-VCH Verlag GmbH & Co. KGaA, Weinheim. (**d**) Optimized configurations for Fe_1-Pyridinic N_4-Pyrrolic O_1. (**e**) LSV curves. (**f**) Faradaic efficiency of CO and H_2. Reprinted with permission from ref. [115]. Copyright: (2021) The Royal Society of Chemistry. (**g**) EXAFS fitting curves of $Ni-N_4-O/C$ in R space. (**h**) LSV curves. (**i**) FE_{CO}. Reprinted with permission from ref. [116]. Copyright: (2020) Wiley-VCH GmbH. (**j**) The side view of the CdN_4S_1 models. Gibbs free energy diagrams for CO_2RR to (**k**) CO and for (**l**) HER with different models. Reprinted with permission from ref. [118]. Copyright: (2021) Wiley-VCH GmbH.

Xie et al. synthesized a neighboring bi-metal atom catalyst (NiN_4-SnN_4) with each Ni and S coordinated with four Ns (Figure 7a). The neighboring Ni redistributes the electrons of Sn and results in the reduced free energy barrier of *OCHO and subsequent thermodynamically spontaneous determining step, and by taking double advantage of the synergistic effect of the NiSn diatomic site and the increased utilization, exhibits excellent selectivity for the generation of formate (86.1% at -0.82 V_{RHE}) compared with Sn-SAC (70.4% at -0.82 V_{RHE}) as well as Ni-SAC (<1 %), as shown in Figure 7b [120]. Hao et al. designed a non-bridged Ni dual-atom catalyst (Ni_2N_6) with a local structure of N_3-Ni-Ni-N_3 for CO_2 to CO (Figure 7c), and in situ environmental STEM captured the Ostwald ripening process of the Ni species generating the bulk phase and the subsequent atomization dynamics process of the transformation into Ni diatomic sites (Figure 7d). The actual active sites for the fast CO_2RR kinetics and the slower HER kinetics are Ni diatomic sites (Ni_2N_6OH) induced via hydroxyl adsorption, according to in situ XAFS studies and theory calculations (Figure 7e). [84] In addition, there is a similar active site on the O-bridge adsorption structure (O-Ni_2N_6) of the 2N-bridged Ni_2N_6 site for the dynamic catalysis of CO_2 [85]. Moreover, several other homoatomic binuclear site catalysts with the special local environment and a non-bridged $Ni_2N_4C_2$ and Pd_2 dual-atom site with a PdN_2O_2 coordination structure have shown superior, nearly 100% CO selectivity [86,121].

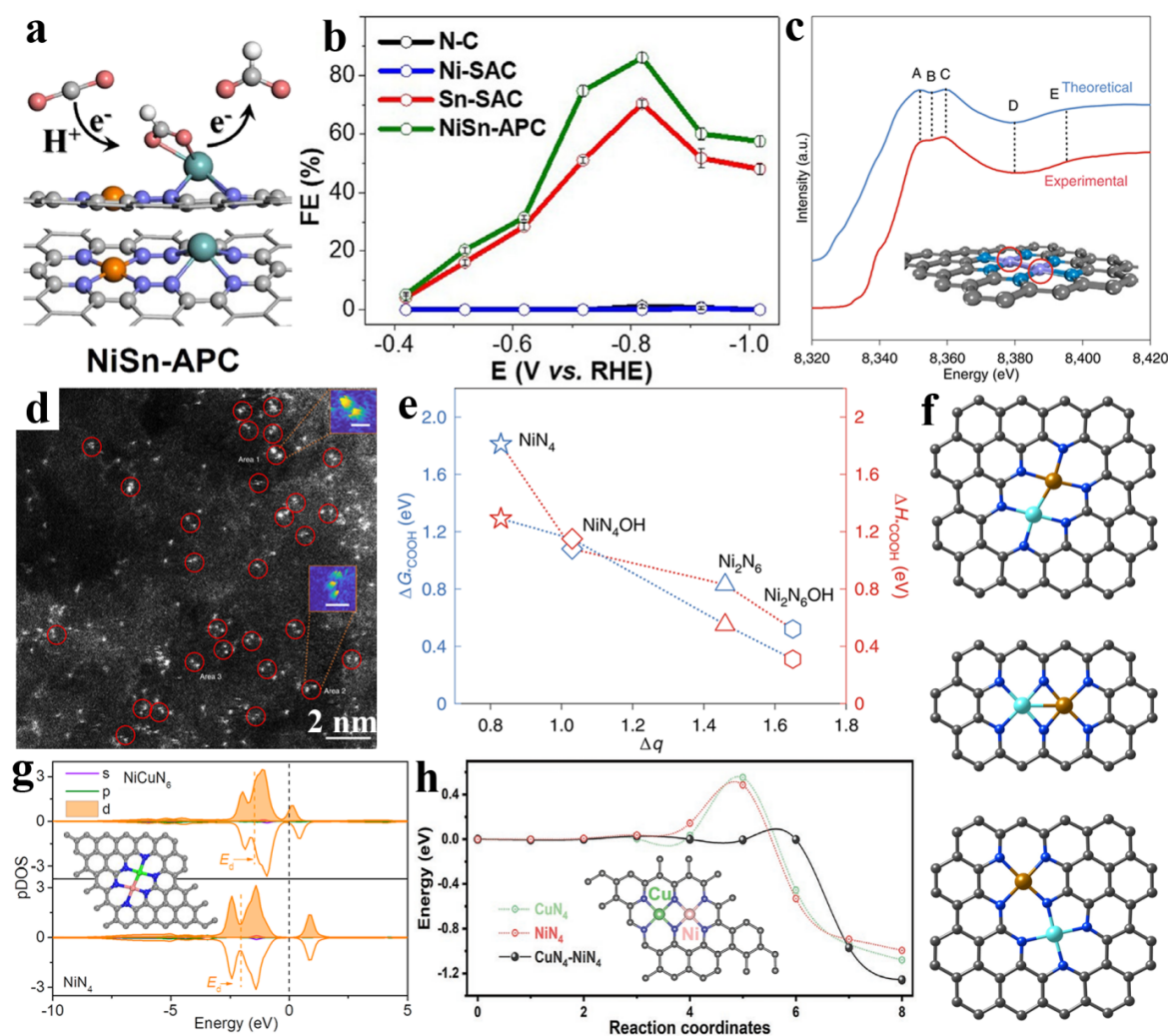**Figure 7.** (**a**) Scheme illustration for CO_2RR of NiSn-APC. (**b**) Faradaic efficiencies for formate. Reprinted with permission from ref. [120]. Copyright: (2020) Wiley-VCH GmbH. (**c**) A comparison between the experimental and the simulated XANES spectra for Ni_2NC. (**d**) The HAADF-STEM images (inset: the Ni-Ni atoms pair. Area 1, 0.25 nm; area 2, 0.5 nm). (**e**) The relationship between Bader

charges (Δq) and Gibbs free energy/Helmholtz free energy for *COOH formation on different sites. Reprinted with permission from ref. [84]. Copyright: (2022) Nature Publishing Group. (**f**) Atomic structure of different dual-metal sites on graphene layer. Reprinted with permission from ref. [122]. Copyright: (2022) Wiley-VCH GmbH. (**g**) Partial density of states (pDOS) of Ni in NiN_4 and $NiCuN_6$. Reprinted with permission from ref. [123]. Copyright: (2022) American Chemical Society. (**h**) Climbing image nudged elastic band (CI-NEB) calculated kinetic reaction processes. Reprinted with permission from ref. [124]. Copyright: (2022) Wiley-VCH GmbH.

To date, some works about the neighboring heterometal $M_1M_2N_x$ sites (M_1/M_2: Fe, Co, Ni, Cu, Zn, etc.) catalysts have been published. Li et al. designed several possible bimetallic site configurations with DFT computational simulations, i.e., non-bridged (Fe-Ni)N_6, 2N-bridged (Fe-Ni)N_6, and 1N-bridged (Fe-Ni)N_7 sites (Figure 7f). The optimal CO_2RR activity and selectivity were identified to be at the 2N-bridged (Fe-Ni)N_6 sites, which can account for these two metal sites' synergistic interaction that could simultaneously promote the adsorption of *COOH and the desorption of *CO while inhibiting the HER [122]. More in-depth insights can be provided through an electronic structure analysis: in the NiFe heteroatom sites, Fe acts as the catalytic center with a higher oxidation state resulting from its orbital coupling with Ni, which facilitates CO_2 activation and does not change the binding strength to *COOH but the weakened binding strength with *CO intermediates, and accelerates CO desorption, thus increasing the catalytic CO_2RR activity [125]. Jiao et al. concluded that in non-bonding Fe_1-Ni_1-N-C, the Fe atomic site can also be highly activated by the adjacent single-atom Ni through non-bonding interactions between them to act as the active center [126]. Meanwhile, Ren et al. believe that the key to the CO_2RR is the collaborative coordination of CO at non-bridged diatomic NiFeN$_6$ sites fixed on nitrogenated carbon [127].

Furthermore, two types of (Cu-Ni)N_6 for non-bridged Ni/Cu-N-C (Figure 7g) and 2N-bridged CuNi-DSA/CNF (inset of Figure 7h) have been reported: for non-bridged Ni/Cu-N-C, the introduction of the secondary Cu metal accelerates the rate-determining step of *COOH formation by transferring the Ni 3d orbital energy to the Fermi energy level; for 2N-bridged CuNi-DSA/CNF, electronegativity shifts between Cu and Ni, causing strong electronic interactions and the offset effect, which can efficiently optimize the adsorption strength of *COOH intermediates. The activation energy of *COOH creation on CuN_4-NiN_4 is 0.08 eV, as shown in Figure 7h, which is much lower than that on CuN_4 and NiN_4 (0.58 eV and 0.48 eV), proving that the CuNi dual-atom sites do actually facilitate the kinetic process of *COOH production [123,124,128]. In addition, co-constructed $M_1M_2N_x$ composed of other metals, e.g., the ZIF-8 containing Fe/Cu sources derived a Cu-Fe diatomic site catalyst that coordinated with the N and was doped in the carbon matrix (non-bridged (Cu-Fe)N_6) [65,67]; direct pyrolysis of a combination of carbon black, metal salt, and a urea nitrogen source yielded a Co-Cu diatomic site catalyst (2N-bridged (Co-Cu)N_6) [129]; a mixture of chitosan and Ni/Zn metal salts derived atomically dispersed Ni-Zn bimetal sites coordinated on N-doped carbon (non-bridged (Ni-Zn)N_6) [130]; and a precursor containing Zn/Co nitrate, urea, and activated carbon black derived diatomic Zn-Co monomers supported on nitrogen-doped carbon (2N-bridged (Zn-Co)N_6) [131], have also shown better CO_2 electroreduction performances.

The analysis of the above different strategies for improving the CO_2RR reveals that each strategy has its own unique advantages, and the combined use of these strategies may achieve unexpected results. It is important to note that the final evaluation index of almost all the strategies focuses on the pair energy barrier and adsorption energy changes due to electronic interactions but ignores factors such as hydrogen bonding, solvation effects, and spatial structure that are often simplified or ignored in theoretical analyses. In addition, mesoscopic factors, such as the modulation of the solid-liquid-gas interface, should also be taken into account.

5.5. Asymmetric Atom Sites of Organic/Metal-Based Supports for CO$_2$RR

Except for carbon-based ones, organic/metal-based supports are also capable of loading the above-mentioned asymmetric coordination atom sites. Organic crystalline materials, including MOFs, covalent organic frameworks (COFs), metal-organic complexes, etc., have explicit structures and tuned metal sites while retaining a major problem of poor electrical conductivity that cannot be ignored.

To overcome the conductivity of a crystallite, one strategy is to enhance conductivity with itself, e.g., conductive MOFs with conjugated organic ligands, and the other is to integrate it with other better conductive materials. Zhang et al. provided coordination-environment-dependent single-site-Cu-O$_4$ conductive MOFs (Cu-DBC), and, by comparing the Cu-N$_4$ sites of two other COFs (Cu-TTCOF and Cu-PPCOF), it can be found that the Cu-O$_4$ site with lower free energy barrier has better CO$_2$ to CH$_4$ activity (Faradaic efficiency of CH$_4$ up to ~80% at -0.9 V vs. RHE) than the CuN$_4$ sites (Figure 8a) [57]. Another conductive COF (PcCu-TFPN) with a high electron density and isolated phthalocyanine CuN$_4$ sites is more appropriate for the critical step of the C-C coupling of *CH$_3$ intermediates with CO$_2$ to generate acetates (Faradaic efficiency of 90.3(2)% at -0.8 V vs. RHE), as shown in Figure 8b [132]. To more precisely elucidate the essential contribution of C-C coupling to the CO$_2$ deep reduction of C$_{2+}$ products, Shao et al. designed two MOFs with various nodes, and, compared with BIF-104 with isolated Cu sites as a reference, BIF-102 for the Cl$^-$ bridging of a dimer Cu unit can provide a higher C$_2$H$_4$ Faraday efficiency as high as ~11.3%, while the adjacent Cu atom acts as a modulator, changing the reaction barrier, promoting C-C coupling, and providing a reaction pathway for generating C$_{2+}$ products that differ from isolated monomers, which shows that there exists a close correlation between the active-centered coordination structure and CO$_2$RR selectivity (Figure 8c) [133]. Zhu et al. hold a comparable view that in robust π–π stacking MOFs (CuBtz) with pyrazolate-bridged dicopper(I) sites, the uncoordinated N atoms act as proton relays and co-catalyze with neighboring Cu sites to promote *CO hydrogenation and the C-C coupling for the highly selective electroreduction of CO$_2$ to C$_{2+}$ products (Figure 8d) [134]. Instead, Lin et al. anchored cobalt phthalocyanine with CoN$_4$ sites (CoPc) in the FeN$_4$ sites of graphene (Fe-N-C) for synergistic catalytic CO$_2$ electroreduction, and the received CoPc@Fe-N-C showed a broader potential window and larger CO current density beyond Fe-N-C [135]. Pan et al. used pre-prepared hollow carbon spheres as supports to successfully construct CoN$_5$ asymmetric sites through the coordination of Co in CoPC and N-doped carbon spheres (Figure 8e), obtaining a high selectivity of FE$_{CO}$ of over 90% for the CO$_2$RR across a broad potential range, from -0.57 V to -0.88 V vs. RHE (Figure 8f) [136]. A similar strategy was successfully employed by Wang et al. to immobilize planar Co^{II}-2,3-naphthalocyanine (NapCo) on graphitic sulfoxide (SO) or carboxyl (COO)-doped graphene (NapCo@graphitic SO; NapCo@COO), i.e., where axial coordination between CoN$_4$ in NapCo and O from SO or COO occurred (Figure 8g). As a result, there was good electronic communication between NapCo and graphene in NapCo@graphitic SO compared with NapCo@COO, resulting in a high Faraday efficiency of 97% for CO production, yet no activity for CO$_2$ electroreduction was found for the CoN$_4$ site of pristine NapCo without graphene [137]. In metal-based supports, Jiao et al. reported Cu$_1^0$-Cu$_1^{x+}$ pairs stabilized on the Te surface imperfections of Pd$_{10}$Te$_3$ alloy nanowires, and, with Cu$_1^{x+}$ and Cu$_1^0$ separately corresponding to the adsorption of molecular H$_2$O and CO$_2$, with an almost completely suppressed HER, this named bi-atomic activating bimolecular effect facilitates the evolution of CO$_2$ to CO (Figure 8h) [138].

Unlike carbon-based supports, there are still relatively few hetero-coordination atoms loaded on organic/metal-based supports, and the key is to fundamentally address organic substrates' conductivity, stability, and lessened selectivity, as well as metallic carriers' undesirable competitive HER, but satisfactory CO$_2$RR data have still been found from the limited reports, which inspires the majority of researchers to continue exploring this vast uncharted territory.
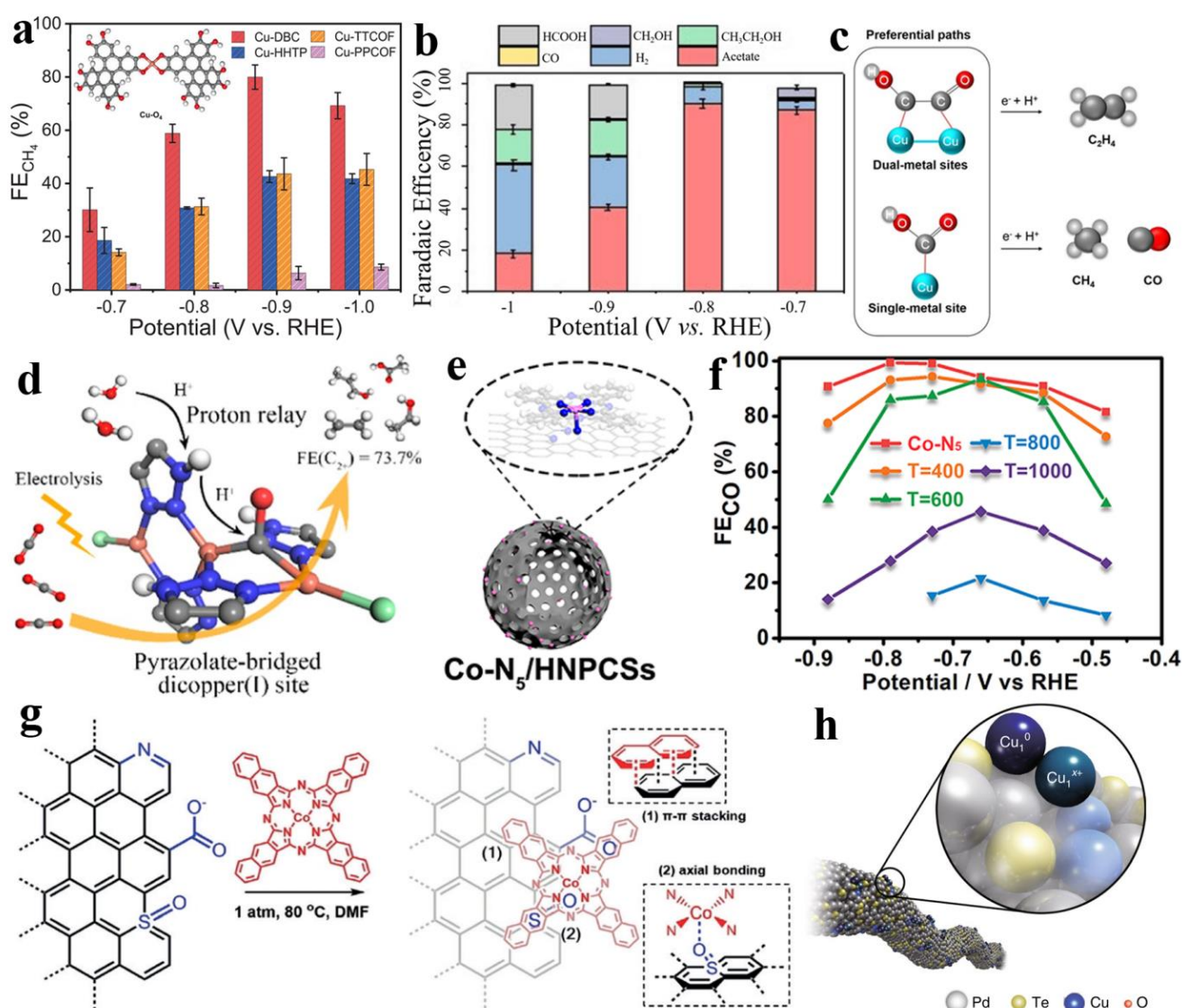
Figure 8. (**a**) Faradaic efficiencies of CH_4 for crystalline single-site Cu electrocatalysts. Reprinted with permission from ref. [57]. Copyright: (2021) Nature Publishing Group. (**b**) Faradaic efficiencies of different CO_2RR products for PcCu-TFPN. Reprinted with permission from ref. [132]. Copyright: (2022) Wiley-VCH GmbH. (**c**) The possible preferential reaction pathways of BIF-102NSs and BIF-104NSs. Reprinted with permission from ref. [133]. Copyright: (2021) Wiley-VCH GmbH. (**d**) The possible reaction process of C_{2+} products for CuBtz. Reprinted with permission from ref. [134]. Copyright: (2022) American Chemical Society. (**e**) Schematic illustration of Co-N_5/HNPCSs. (**f**) FE_{CO}. Reprinted with permission from ref. [136]. Copyright: (2018) American Chemical Society. (**g**) Heterogenization of NapCo onto doped-graphene through p-p stacking and coordination with heteroatoms. Reprinted with permission from ref. [137]. Copyright: (2019) Wiley-VCH Verlag GmbH & Co. KGaA, Weinheim. (**h**) Schematic illustration of Cu atom pair anchored on $Pd_{10}Te_3$ nanowires. Reprinted with permission from ref. [138]. Copyright: (2019) Nature Publishing Group.

6. Summary and Outlook

For over a decade, significant advancements have been accomplished in the structural design and fundamental electrocatalytic investigation of SACs as next-generation catalysts with a maximum of nearly 100% atomic utilization [139–141]. However, for the CO_2RR, the simplicity of the conventional MN_4 structure severely restricts the substantial improvement of its electrocatalytic activity. It is commonly accepted that the SACs' coordination structures determine the electronic structures and thus affect the intrinsic electrocatalytic activity.

It follows that the local/expanded coordination environment of active single atoms in SACs has a combined effect on the stability, catalytic performance, and utilization of the loaded materials [142,143]. As shown in Table 1, asymmetric atom sites, which have recently gained popularity among a wide range of researchers, can provide flexible structures with customizable atomic configuration, local/expanded coordination, and electronic architecture without damaging this principle of high atomic utilization, thereby breaking such innate limitations of MN_4. Therefore, efforts have been made in recent years to develop more advanced asymmetric atom electrocatalysts for the CO_2RR compared with SACs.

Table 1. The comparison of CO_2RR performances of the SACs with different active sites.

Catalyst	Active Site	Electrolyte	Product, FE (%)	Current Density (mA cm^{-2}) (E vs. RHE)	Ref.
Fe_1NC/S_1_800	FeN_4	0.5 M $KHCO_3$	CO, 82	~2.9 (-0.5 V)	[66]
NiN_4	NiN_4	0.5 M $KHCO_3$	CO, ~80	~15 (-0.9 V)	[71]
Fe_1NC/S_1_1000	FeN_3	0.5 M $KHCO_3$	CO, 96	6.4 (-0.5 V)	[66]
NiN_3V	NiN_3	0.5 M $KHCO_3$	CO, >90	~60 (-0.9 V)	[71]
$Mn–C_3N_4/CNT$	MnN_3	0.5 M $KHCO_3$	CO, 98.8	14 (-0.55 V)	[101]
Ni SAs/N-C	NiN_3C_1	0.5 M $KHCO_3$	CO, 71.9	10.48 (-1.0 V)	[102]
$NiSA-N_2-C$	NiN_2C_2	0.5 M $KHCO_3$	CO, ~100	~12 (-0.8 V)	[103]
Single-atom $Sn^{\delta+}$ on N-doped graphene	SnN_2C_2	0.25 M $KHCO_3$	Formate, 74.3	11.7 (-1.6 V_{SCE})	[106]
Sn-NOC	SnN_3O_1	0.1 M $KHCO_3$	CO, 94	13.9 (-0.7 V)	[64]
Bi-SAs-NS/C	BiN_3S_1	0.5 M $KHCO_3$	CO, 98.3	~10 (-0.8 V)	[108]
FeN_5	FeN_4N_1	0.1 M $KHCO_3$	CO, 97	~5 (-0.46 V)	[114]
$Fe-CON_{400}\_400$	FeN_4O_1	0.1 M $KHCO_3$	CO, ~100	~15 ($-0.56\sim-0.87$ V)	[115]
$Ni-N_4-O/C$	NiN_4O_1	0.5 M $KHCO_3$	CO, >90	~30 ($-0.5\sim-0.1.1$ V)	[116]
NiSn-APC	NiN_4-SnN_4	0.5 M $KHCO_3$	Formate, 86.1	~22 (-0.82 V)	[120]
ZIF-NC-Ni-Fe	2N-bridged $FeNiN_6$	0.1 M $KHCO_3$	CO, >93	~22 ($-0.3\sim-1.0$)	[122]
Ni/Cu-N-C	Non-bridged $NiCuN_6$	0.5 M $KHCO_3$	CO, 97.7	~13.7 (-0.6 V)	[123]

Furthermore, the attention on the CO_2RR has extended to the catalytic environment, as the catalytic activity can be modulated by altering the structural parameters of the catalyst (solid)-electrolyte (liquid)-molecular reactant (gas) three-phase interface [144–146]. Some advances have been realized in these interfacial modulation studies, wherein it was discovered that controlling the proton supply or CO_2 supply can effectively inhibit the HER [147,148], electrodes with improved interfacial structures significantly improve selectivity and partial current density at relatively low overpotentials in H-type electrolytic cells [149,150], and membrane reactors and microfluidic reactors (flow cells) can achieve higher current densities [151,152]. Modification of the catalyst-electrolyte interface region also includes the addition of external molecules (or polymers), changes in electrolyte composition and concentration, the design of novel reactor and electrode structures, and a combination of these approaches, and these modification strategies can significantly affect the intrinsic and extrinsic catalytic activity of the catalyst. Furthermore, the design of syngas (H_2 and CO) catalysts can also give us some guidance, especially by regulating the relative content of different active center species, to achieve the selectivity of H_2 and CO, which can be used to determine the differences in various activities of metal sites for the CO_2RR and HER and to obtain general design principles [153,154]. Moreover, some predictions about CO_2RR electrocatalysts from theoretical calculations also provide guidance for the development of new catalysts, which have previously received less attention, for example, Rh@Au(100) and Rh@Ag(100), which may produce CH_4 [155], and the Cu_2N_4-loaded C_2N layer, which can form CH_4 and C_2H_4 [156], are expected to perform well.

Recent studies on asymmetric atom sites in the electrocatalysis of the CO_2RR were reviewed in this paper, with importance placed on the comparison of asymmetric atom sites and traditional SACs for the CO_2RR, including an examination of the crucial role that coordination structures play in the intrinsic electrocatalytic activity of supports-loaded SACs, including local coordination (metal atom center and first coordination shell) and extended coordination (second and higher coordination shell), as well as the resulting alternation

in the adsorption parameters, the decrease in the energy barrier of rate-determining step, and the optimization of the reaction pathway. It can be straightforwardly found that asymmetric atom sites have significant advantages in improving the electrocatalytic properties when performing the CO_2RR over symmetrical atomic catalysts, including catalytic activity, Faraday efficiency, selectivity, stability, etc. It is worth noting that, for the CO_2RR, this is a universal rule, but some prominent properties of the symmetric coordination should not be neglected, and thus it is concluded that asymmetric atom catalysts are expected to break the theoretical boundary of SACs [157,158]. Furthermore, we proposed the current urgent challenges to be solved and future expected directions in the field of asymmetric atom sites.

The accurate management of single atoms' desired coordination environments on the supports remains a major challenge. After the coordination environment is optimized, the corresponding active monoatom is securely trapped in the surface anchor site via the charge transfer effect, interaction absorption, etc., which could successfully avoid the metal atom movement and agglomeration caused by high surface energy during the construction procedure and reaction system, impairing its catalytic efficacy [159–161]. Currently, SACs with outstanding performance have been successfully established using some reported synthetic approaches, including wet chemistry, ALD deposition, and high-temperature pyrolysis. However, metal nanoclusters or even NPs are occasionally doped into the resultant SACs. The conventional wet impregnation methods are easy to implement, low-cost, and have a scalable production, but obtaining highly loaded and precisely regulated single-atom coordinated sites is challenging [162–164]. The popular high-temperature pyrolysis method generally involves the high-temperature calcination of a pre-designed precursor, but it often has unpredictable and ill-defined multiple coordination structures simultaneously due to the influence of the pyrolysis temperature, heating rate, inert atmosphere, and other factors [165–167]. The ALD method, which has the advantage of high-precision control procedures, also has the non-negligible disadvantages of complex synthesis steps, a handful of substrate selection, high investment, and low productivity [168–170]. Not negligibly, a suitable choice of supports species will influence the vacancies and defects on the surface to be better utilized for stabilizing isolated metal atoms. Carbon-based materials have become the main choice of carriers for SACs due to the easy introduction of O, S, and N elements, but a major drawback is the instability of carbon-based materials at high temperatures and high oxygen concentrations [171–174]. Correspondingly, the field of supports should be expanded, such as organic crystallization, metals, and derived oxides and nitrides, as well as the selection of the best preparation techniques. Practically speaking, further breakthroughs in the field of SACs lie in the updating of low-cost, easily scalable, and environmentally friendly preparation methods [175–180].

Accurate identification of the coordination environment is essential for the development of SACs. STEM techniques allow direct viewing of individual metal atoms to obtain relatively well-defined coordination structures, but the low Z-contrast of the first/second coordination shell (e.g., C, N, S, etc.) causes considerable trouble in mapping the spatial positions of the near-end light atoms. In addition, XAFS characterization can directly distinguish between metal NPs and atomically dispersed atoms, but the acquired coordination structure is generally an averaged result [178–185]. Currently, a combination of characterization techniques, such as electron energy loss spectroscopy (EDS), X-ray photoelectron spectroscopy (XPS), scanning tunneling microscopy (STM), non-contact atomic force microscopy (AFM), and DFT theoretical modeling, is required to obtain a relatively reliable local structure determination [181–189]. With the emergence of various in situ/operando characterization techniques in recent years, it has become feasible to directly monitor catalytic reaction processes, which would be extremely potent if applied in conjunction with advanced theoretical modeling. For example, the conversion of dispersed metal atoms into clusters or NPs during electrolysis has been confirmed [184]. A comprehensive insight into the structure-property connection relies on the expression of isolated single atoms rather than statistically averaging data of all the single atoms in diverse bonding structure distributions. The combination of electron microscopy techniques, spectral analysis, and DFT

calculations can, firstly, reflect the nature of a single-atom configuration, then, recognize the dynamic evolution of the active components during the formation of products, and, finally, make the reaction pathway and mechanism gradually clear, which is of major interest for catalyst design [190–195].

Large-scale industrial applications require the batch construction of SACs with high activity and selectivity using simple and scalable methods, whereby the ultimate goal is to switch out the current noble metal-based electrocatalysts with more accessible transition metals, which is advantageous for the atomic economy and the advancement of green chemistry [188–198]. A practical screening tool is machine learning, which enables the matching and integration of different elements or groups, model construction, and the specific performance prediction of catalysts, and then obtaining optimal results using high-throughput screening, these methods greatly reduce the investment of time and human, material, and financial resources [199–203]. In addition, the factor of long-term thermodynamic stability also needs to be considered [204,205]. Too strong or too weak interactions in the metal-species-anchored supports systems during catalysis can result in negative Ostwald maturation and the migration and aggregation of active sites, respectively [206,207]. In particular, the high temperatures and reducing environments usually faced in industrial applications make catalysts more vulnerable to poisoning or deactivation [199,207]. Overall, the design of high-quality asymmetric atom electrocatalysts via reasonable coordination modulation remains promising.

Author Contributions: Writing—original draft preparation, X.H. and J.D.; writing—review and editing, W.L., S.Z. and J.L.; supervision, X.L. All authors have read and agreed to the published version of the manuscript.

Data Availability Statement: No new data were created or analyzed in this study. Data sharing is not applicable to this article.

Conflicts of Interest: The authors declare no conflict of interest.

References

1. Zhang, H.L.; Mu, J.E.; McCarl, B.A.; Yu, J.L. The impact of climate change on global energy use. *Mitig. Adapt. Strateg. Glob. Change* **2022**, *27*, 9. [CrossRef]
2. Wang, L.G.; Duan, X.X.; Liu, X.J.; Gu, J.; Si, R.; Qiu, Y.; Qiu, Y.M.; Shi, D.E.; Chen, F.H.; Sun, X.M.; et al. Atomically Dispersed Mo Supported on Metallic Co$_9$S$_8$ Nanoflakes as an Advanced Noble-Metal-Free Bifunctional Water Splitting Catalyst Working in Universal pH Conditions. *Adv. Energy Mater.* **2020**, *10*, 1903137. [CrossRef]
3. Liang, C.; Shuaibo, Z.; Waqar, A.; Jing, Z.; Yue, Z.; Wensheng, Y.; Yongfang, L. High-performance large-area perovskite photovoltaic modules. *Nano Res. Energy* **2022**, *1*, e9120024.
4. Khan, S.A.R.; Ponce, P.; Yu, Z.; Ponce, K. Investigating economic growth and natural resource dependence: An asymmetric approach in developed and developing economies. *Resour. Policy* **2022**, *77*, 102672. [CrossRef]
5. Sen, W.; Jiaxin, M.; Xiaoyu, S.; Yuanyuan, Z.; Zhong-Shuai, W. Recent status and future perspectives of ultracompact and customizable micro-supercapacitors. *Nano Res. Energy* **2022**, *1*, e9120018.
6. Winter, R.A. Innovation and the dynamics of global warming. *J. Environ. Econ. Manag.* **2014**, *68*, 124–140. [CrossRef]
7. Guojin, L.; Xinliang, L.; Yanbo, W.; Shuo, Y.; Zhaodong, H.; Qi, Y.; Donghong, W.; Binbin, D.; Minshen, Z.; Chunyi, Z.; et al. Building durable aqueous K-ion capacitors based on MXene family. *Nano Res. Energy* **2022**, *1*, e9120002.
8. Kirikkaleli, D.; Sowah, J.K. Time-frequency dependency of temperature and sea level: A global perspective. *Environ. Sci. Pollut. Res.* **2021**, *28*, 58787–58798. [CrossRef]
9. Adebayo, T.S.; Onifade, S.T.; Alola, A.A.; Muoneke, O.B. Does it take international integration of natural resources to ascend the ladder of environmental quality in the newly industrialized countries? *Resour. Policy* **2022**, *76*, 102616. [CrossRef]
10. Jie, Z.; Leyu, B.; Yuanhang, C.; Baomin, X.; Alex, K.Y.J. Self-assembled monolayer enabling improved buried interfaces in blade-coated perovskite solar cells for high efficiency and stability. *Nano Energy* **2022**, *1*, e9120004.
11. Hou, J.; Peng, X.; Sun, J.; Zhang, S.; Liu, Q.; Wang, X.; Luo, J.; Liu, X. Accelerating hydrazine-assisted hydrogen production kinetics with Mn dopant modulated CoS$_2$ nanowire arrays. *Inorg. Chem. Front.* **2022**, *9*, 3047–3058. [CrossRef]
12. Strmcnik, D.; Lopes, P.P.; Genorio, B.; Stamenkovic, V.R.; Markovic, N.M. Design principles for hydrogen evolution reaction catalyst materials. *Nano Energy* **2016**, *29*, 29–36. [CrossRef]

13. Chen, H.; Zhang, S.; Liu, Q.; Yu, P.; Luo, J.; Hu, G.; Liu, X. CoSe$_2$ nanocrystals embedded into carbon framework as efficient bifunctional catalyst for alkaline seawater splitting. *Inorg. Chem. Commun.* **2022**, *146*, 110170. [CrossRef]

14. Peng, L.S.; Yang, N.; Yang, Y.Q.; Wang, Q.; Xie, X.Y.; Sun-Waterhouse, D.; Shang, L.; Zhang, T.R.; Waterhouse, G.I.N. Atomic Cation-Vacancy Engineering of NiFe-Layered Double Hydroxides for Improved Activity and Stability towards the Oxygen Evolution Reaction. *Angew. Chem.* **2021**, *60*, 24612–24619. [CrossRef]

15. Wang, H.J.; Wang, W.X.; Yu, H.J.; Mao, Q.Q.; Xu, Y.; Li, X.N.; Wang, Z.Q.; Wang, L. Interface engineering of polyaniline-functionalized porous Pd metallene for alkaline oxygen reduction reaction. *Appl. Catal. B Environ.* **2022**, *307*, 121172. [CrossRef]

16. Qi, G.C.; Zhao, Q.R.; Liu, Q.J.; Fang, D.Y.; Liu, X.J. Biomass-derived carbon frameworks for oxygen and carbon dioxide electrochemical reduction. *Ionics* **2021**, *27*, 3579–3586. [CrossRef]

17. Lulu, L.; ul Hasan, I.M.; Farwa; Ruinan, H.; Luwei, P.; Nengneng, X.; Nabeel Khan, N.; Jia-Nan, Z.; Jinli, Q. Copper as a single metal atom based photo-, electro-, and photoelectrochemical catalyst decorated on carbon nitride surface for efficient CO$_2$ reduction: A review. *Nano Res. Energy* **2022**, *1*, e9120015.

18. Gao, S.; Wang, T.; Jin, M.; Zhang, S.; Liu, Q.; Hu, G.; Yang, H.; Luo, J.; Liu, X. Bifunctional Nb-N-C atomic catalyst for aqueous Zn-air battery driving CO$_2$ electrolysis. *Sci. China Mater.* **2022**, *65*, 1–11. [CrossRef]

19. Ge, M.; Mengmeng, J.; Tianran, W.; Qian, L.; Shusheng, Z.; Xianyun, P.; Jun, L.; Xijun, L. MoC nanocrystals confined in N-doped carbon nanosheets toward highly selective electrocatalytic nitric oxide reduction to ammonia. *Nano Res.* **2022**, *15*, 8890–8896.

20. Qian, X.; Ma, C.Q.; Shahid, U.B.; Sun, M.J.; Zhang, X.L.; Tian, J.; Shao, M.H. Synergistic Enhancement of Electrocatalytic Nitrogen Reductionover Few-Layer MoSe$_2$-Decorated Ti$_3$C$_2$Tx MXene. *ACS Catal.* **2022**, *12*, 6385–6393. [CrossRef]

21. Defeng, Q.; Fang, L.; Tianran, W.; Mengmeng, J.; Ge, M.; Shusheng, Z.; Qian, L.; Wenxian, L.; Dui, M.; Mohamed, S.; et al. High-efficiency electrocatalytic NO reduction to NH$_3$ by nanoporous VN. *Nano Res. Energy* **2022**, *1*, e9120022.

22. Geng, J.; Ji, S.; Jin, M.; Zhang, C.; Xu, M.; Wang, G.; Liang, C.; Zhang, H. Ambient Electrosynthesis of Urea with Nitrate and Carbon Dioxide over Iron-Based Dual-Sites. *Angew. Chem.* **2023**, e202210958. [CrossRef]

23. Jiawei, G.; Yi, P.; Ting, Z.; Jiao, M.; Huan, P.; Yusuke, Y. Porphyrin-based framework materials for energy conversion. *Nano Res. Energy* **2022**, *1*, e9120009.

24. Ding, J.; Yang, H.; Zhang, S.; Liu, Q.; Cao, H.; Luo, J.; Liu, X. Advances in the Electrocatalytic Hydrogen Evolution Reaction by Metal Nanoclusters-based Materials. *Small* **2022**, *18*, 2204524. [CrossRef] [PubMed]

25. Wang, L.; Wang, D.; Li, Y. Single-atom catalysis for carbon neutrality. *Carbon Energy* **2022**, *4*, 1021–1079. [CrossRef]

26. Yu, X.; Deng, J.; Liu, Y.; Jing, L.; Hou, Z.; Pei, W.; Dai, H. Single-Atom Catalysts: Preparation and Applications in Environmental Catalysis. *Catalysts* **2022**, *12*, 1239. [CrossRef]

27. Guo, X.; Wan, X.; Shui, J. Molybdenum-based materials for electrocatalytic nitrogen reduction reaction. *Cell Rep. Phys. Sci.* **2021**, *2*, 100447. [CrossRef]

28. Hairong, X.; Hao, G.; Yusuke, Y.; Takayoshi, S.; Renzhi, M. Photo-enhanced rechargeable high-energy-density metal batteries for solar energy conversion and storage. *Nano Res. Energy* **2022**, *1*, e9120007.

29. Yang, M.S.; Liu, S.; Sun, J.Q.; Jin, M.M.; Fu, R.; Zhang, S.S.; Li, H.Y.; Sun, Z.Y.; Luo, J.; Liu, X.J.; et al. Highly dispersed Bi clusters for efficient rechargeable Zn-CO$_2$ batteries. *Appl. Catal. B Environ.* **2022**, *307*, 121145. [CrossRef]

30. Han, L.L.; Song, S.J.; Liu, M.J.; Yao, S.Y.; Liang, Z.X.; Cheng, H.; Ren, Z.H.; Liu, W.; Lin, R.Q.; Qi, G.C.; et al. Stable and Efficient Single-Atom Zn Catalyst for CO$_2$ Reduction to CH$_4$. *J. Am. Chem. Soc.* **2020**, *142*, 12563–12567. [CrossRef]

31. Sun, T.; Mitchell, S.; Li, J.; Lyu, P.; Wu, X.; Perez-Ramirez, J.; Lu, J. Design of Local Atomic Environments in Single-Atom Electrocatalysts for Renewable Energy Conversions. *Adv. Mater.* **2021**, *33*, 2003075. [CrossRef]

32. Shen, T.; Wang, S.; Zhao, T.; Hu, Y.; Wang, D. Recent Advances of Single-Atom-Alloy for Energy Electrocatalysis. *Adv. Energy Mater.* **2022**, *12*, 2201823. [CrossRef]

33. Qiao, B.T.; Wang, A.Q.; Yang, X.F.; Allard, L.F.; Jiang, Z.; Cui, Y.T.; Liu, J.Y.; Li, J.; Zhang, T. Single-atom catalysis of CO oxidation using Pt$_1$/FeO$_x$. *Nat. Chem.* **2011**, *3*, 634–641. [CrossRef]

34. Liu, H.; Peng, X.; Liu, X. Single-Atom Catalysts for the Hydrogen Evolution Reaction. *ChemElectroChem* **2018**, *5*, 2963–2974. [CrossRef]

35. Li, R.Z.; Wang, D.S. Understanding the structure-performance relationship of active sites at atomic scale. *Nano Res.* **2022**, *15*, 6888–6923. [CrossRef]

36. Liang, Z.W.; Shen, J.D.; Xu, X.J.; Li, F.K.; Liu, J.; Yuan, B.; Yu, Y.; Zhu, M. Advances in the Development of Single-Atom Catalysts for High-Energy-Density Lithium-Sulfur Batteries. *Adv. Mater.* **2022**, *34*, 2200102. [CrossRef]

37. Zhang, Q.; Zhang, S.; Luo, Y.; Liu, Q.; Luo, J.; Chu, P.; Liu, X. Preparation of high entropy alloys and application to catalytical water electrolysis. *APL Mater.* **2022**, *10*, 070701. [CrossRef]

38. Zheng, X.B.; Li, B.B.; Wang, Q.S.; Wang, D.S.; Li, Y.D. Emerging low-nuclearity supported metal catalysts with atomic level precision for efficient heterogeneous catalysis. *Nano Res.* **2022**, *15*, 7806–7839. [CrossRef]

39. Wu, D.H.; He, B.L.; Wang, Y.Y.; Lv, P.; Ma, D.W.; Jia, Y. Double-atom catalysts for energy-related electrocatalysis applications: A theoretical perspective. *J. Phys. D Appl. Phys.* **2022**, *55*, 203001. [CrossRef]

40. Mi, Y.Y.; Qiu, Y.; Liu, Y.F.; Peng, X.N.; Hu, M.; Zhao, S.Z.; Cao, H.Q.; Zhuo, L.C.; Li, H.Y.; Ren, J.Q.; et al. Cobalt-Iron Oxide Nanosheets for High-Efficiency Solar-Driven CO$_2$-H$_2$O Coupling Electrocatalytic Reactions. *Adv. Funct. Mater.* **2020**, *30*, 2003438. [CrossRef]

41. Liu, H.; Fu, J.; Li, H.; Sun, J.; Liu, X.; Qiu, Y.; Peng, X.; Liu, Y.; Bao, H.; Zhuo, L.; et al. Single palladium site in ordered porous heteroatom-doped carbon for high-performance alkaline hydrogen oxidation. *Appl. Catal. B Environ.* **2022**, *306*, 121029. [CrossRef]

42. Zhu, P.; Xiong, X.; Wang, D.S. Regulations of active moiety in single atom catalysts for electrochemical hydrogen evolution reaction. *Nano Res.* **2022**, *15*, 5792–5815. [CrossRef]

43. Li, J.H.; Li, Q.L.; Zhao, L.; Zhang, J.H.; Tang, X.; Gu, L.X.; Guo, Q.; Ma, H.X.; Zhou, Q.; Liu, Y.; et al. Rapid screening of Zr-containing particles from Chang'e-5 lunar soil samples for isotope geochronology: Technical roadmap for future study. *Geosci. Front.* **2022**, *13*, 101367. [CrossRef]

44. Meng, G.; Cao, H.; Wei, T.; Liu, Q.; Fu, J.; Zhang, S.; Luo, J.; Liu, X. Highly dispersed Ru clusters toward an efficient and durable hydrogen oxidation reaction. *Chem. Commun.* **2022**, *58*, 11839–11842. [CrossRef] [PubMed]

45. Shi, X.W.; Dai, C.; Wang, X.; Hu, J.Y.; Zhang, J.Y.; Zheng, L.X.; Mao, L.; Zheng, H.J.; Zhu, M.S. Protruding Pt single-sites on hexagonal ZnIn$_2$S$_4$ to accelerate photocatalytic hydrogen evolution. *Nat. Commun.* **2022**, *13*, 1287. [CrossRef] [PubMed]

46. Yang, M.S.; Liu, Y.F.; Sun, J.Q.; Zhang, S.S.; Liu, X.J.; Luo, J. Integration of partially phosphatized bimetal centers into trifunctional catalyst for high-performance hydrogen production and flexible Zn-air battery. *Sci. China Mater.* **2022**, *65*, 1176–1186. [CrossRef]

47. Peng, X.Y.; Zhao, S.Z.; Mi, Y.Y.; Han, L.L.; Liu, X.J.; Qi, D.F.; Sun, J.Q.; Liu, Y.F.; Bao, H.H.; Zhuo, L.C.; et al. Trifunctional Single-Atomic Ru Sites Enable Efficient Overall Water Splitting and Oxygen Reduction in Acidic Media. *Small* **2020**, *16*, 2002888. [CrossRef]

48. Yan, H.; Zhao, M.Y.; Feng, X.; Zhao, S.M.; Zhou, X.; Li, S.F.; Zha, M.H.; Meng, F.Y.; Chen, X.B.; Liu, Y.B.; et al. PO$_4^{3-}$ Coordinated Robust Single-Atom Platinum Catalyst for Selective Polyol Oxidation. *Angew. Chem.* **2022**, *134*, e202116059. [CrossRef]

49. Xia, T.; Wan, J.W.; Yu, R.B. Progress of the Structure-property Correlation of Heteroatomic Coordination Structured Carbon-based Single-atom Electrocatalysts. *Chem. J. Chin. Univ.* **2022**, *43*, 20220162.

50. Gu, H.; Wu, J.; Zhang, L. Recent advances in the rational design of single-atom catalysts for electrochemical CO$_2$ reduction. *Nano Res.* **2022**, *15*, 9747–9763. [CrossRef]

51. Zhang, H.; Jin, X.; Lee, J.M.; Wang, X. Tailoring of Active Sites from Single to Dual Atom Sites for Highly Efficient Electrocatalysis. *ACS Nano* **2022**, *16*, 17572. [CrossRef]

52. Chen, Y.; Lin, J.; Jia, B.; Wang, X.; Jiang, S.; Ma, T. Isolating Single and Few Atoms for Enhanced Catalysis. *Adv. Mater.* **2022**, *34*, e2201796. [CrossRef]

53. Peng, L.; Shang, L.; Zhang, T.; Waterhouse, G.I.N. Recent Advances in the Development of Single-Atom Catalysts for Oxygen Electrocatalysis and Zinc–Air Batteries. *Adv. Energy Mater.* **2020**, *10*, 2003018. [CrossRef]

54. Li, R.; Wang, D. Superiority of Dual-Atom Catalysts in Electrocatalysis: One Step Further Than Single-Atom Catalysts. *Adv. Energy Mater.* **2022**, *12*, 2103564. [CrossRef]

55. Tang, T.; Wang, Z.; Guan, J. Optimizing the Electrocatalytic Selectivity of Carbon Dioxide Reduction Reaction by Regulating the Electronic Structure of Single-Atom M-N-C Materials. *Adv. Funct. Mater.* **2022**, *32*, 2111504. [CrossRef]

56. Zhang, B.; Zhang, J.; Shi, J.; Tan, D.; Liu, L.; Zhang, F.; Lu, C.; Su, Z.; Tan, X.; Cheng, X.; et al. Manganese acting as a high-performance heterogeneous electrocatalyst in carbon dioxide reduction. *Nat. Commun.* **2019**, *10*, 2980. [CrossRef]

57. Zhang, Y.; Dong, L.Z.; Li, S.; Huang, X.; Chang, J.N.; Wang, J.H.; Zhou, J.; Li, S.L.; Lan, Y.Q. Coordination environment dependent selectivity of single-site-Cu enriched crystalline porous catalysts in CO$_2$ reduction to CH$_4$. *Nat. Commun.* **2021**, *12*, 6390. [CrossRef]

58. Varela, A.S.; Ranjbar Sahraie, N.; Steinberg, J.; Ju, W.; Oh, H.S.; Strasser, P. Metal-Doped Nitrogenated Carbon as an Efficient Catalyst for Direct CO$_2$ Electroreduction to CO and Hydrocarbons. *Angew. Chem.* **2015**, *54*, 10758–10762. [CrossRef]

59. Shen, J.; Kortlever, R.; Kas, R.; Birdja, Y.Y.; Diaz-Morales, O.; Kwon, Y.; Ledezma-Yanez, I.; Schouten, K.J.P.; Mul, G.; Koper, M.T.M.; et al. Electrocatalytic reduction of carbon dioxide to carbon monoxide and methane at an immobilized cobalt protoporphyrin. *Nat. Commun.* **2015**, *6*, 8177. [CrossRef]

60. Bi, W.; Li, X.; You, R.; Chen, M.; Yuan, R.; Huang, W.; Wu, X.; Chu, W.; Wu, C.; Xie, Y. Surface Immobilization of Transition Metal Ions on Nitrogen-Doped Graphene Realizing High-Efficient and Selective CO$_2$ Reduction. *Adv. Mater.* **2018**, *30*, 1706617. [CrossRef]

61. Tripkovic, V.; Vanin, M.; Karamad, M.; Björketun, M.E.; Jacobsen, K.W.; Thygesen, K.S.; Rossmeisl, J. Electrochemical CO$_2$ and CO Reduction on Metal-Functionalized Porphyrin-like Graphene. *J. Phys. Chem. C* **2013**, *117*, 9187–9195. [CrossRef]

62. Zhang, C.; Yang, S.; Wu, J.; Liu, M.; Yazdi, S.; Ren, M.; Sha, J.; Zhong, J.; Nie, K.; Jalilov, A.S.; et al. Electrochemical CO$_2$ Reduction with Atomic Iron-Dispersed on Nitrogen-Doped Graphene. *Adv. Energy Mater.* **2018**, *8*, 1703487. [CrossRef]

63. Huan, T.N.; Ranjbar, N.; Rousse, G.; Sougrati, M.; Zitolo, A.; Mougel, V.; Jaouen, F.; Fontecave, M. Electrochemical Reduction of CO$_2$ Catalyzed by Fe-N-C Materials: A Structure–Selectivity Study. *ACS Catal.* **2017**, *7*, 1520–1525. [CrossRef]

64. Guo, J.; Zhang, W.; Zhang, L.H.; Chen, D.; Zhan, J.; Wang, X.; Shiju, N.R.; Yu, F. Control over Electrochemical CO$_2$ Reduction Selectivity by Coordination Engineering of Tin Single-Atom Catalysts. *Adv. Sci.* **2021**, *8*, 2102884. [CrossRef] [PubMed]

65. Yun, R.; Zhan, F.; Wang, X.; Zhang, B.; Sheng, T.; Xin, Z.; Mao, J.; Liu, S.; Zheng, B. Design of Binary Cu–Fe Sites Coordinated with Nitrogen Dispersed in the Porous Carbon for Synergistic CO$_2$ Electroreduction. *Small* **2021**, *17*, 2006951. [CrossRef]

66. Wang, T.; Sang, X.; Zheng, W.; Yang, B.; Yao, S.; Lei, C.; Li, Z.; He, Q.; Lu, J.; Lei, L.; et al. Gas Diffusion Strategy for Inserting Atomic Iron Sites into Graphitized Carbon Supports for Unusually High-Efficient CO$_2$ Electroreduction and High-Performance Zn–CO$_2$ Batteries. *Adv. Mater.* **2020**, *32*, 2002430. [CrossRef]

67. Feng, M.; Wu, X.; Cheng, H.; Fan, Z.; Li, X.; Cui, F.; Fan, S.; Dai, Y.; Lei, G.; He, G. Well-defined Fe–Cu diatomic sites for efficient catalysis of CO_2 electroreduction. *J. Mater. Chem. A* **2021**, *9*, 23817–23827. [CrossRef]

68. Li, S.; Zhao, S.; Lu, X.; Ceccato, M.; Hu, X.M.; Roldan, A.; Catalano, J.; Liu, M.; Skrydstrup, T.; Daasbjerg, K.; et al. Low-Valence $Zn^{\delta+}$ ($0<\delta<2$) Single-Atom Material as Highly Efficient Electrocatalyst for CO_2 Reduction. *Angew. Chem.* **2021**, *60*, 22826–22832.

69. Liu, X.; Zheng, L.; Han, C.; Zong, H.; Yang, G.; Lin, S.; Kumar, A.; Jadhav, A.R.; Tran, N.Q.; Hwang, Y.; et al. Identifying the Activity Origin of a Cobalt Single-Atom Catalyst for Hydrogen Evolution Using Supervised Learning. *Adv. Funct. Mater.* **2021**, *31*, 2100547. [CrossRef]

70. Qiu, H.J.; Ito, Y.; Cong, W.; Tan, Y.; Liu, P.; Hirata, A.; Fujita, T.; Tang, Z.; Chen, M. Nanoporous Graphene with Single-Atom Nickel Dopants: An Efficient and Stable Catalyst for Electrochemical Hydrogen Production. *Angew. Chem.* **2015**, *54*, 14031–14035. [CrossRef]

71. Rong, X.; Wang, H.J.; Lu, X.L.; Si, R.; Lu, T.B. Controlled Synthesis of a Vacancy-Defect Single-Atom Catalyst for Boosting CO_2 Electroreduction. *Angew. Chem.* **2020**, *59*, 1961–1965. [CrossRef]

72. Jia, C.; Li, S.; Zhao, Y.; Hocking, R.K.; Ren, W.; Chen, X.; Su, Z.; Yang, W.; Wang, Y.; Zheng, S.; et al. Nitrogen Vacancy Induced Coordinative Reconstruction of Single-Atom Ni Catalyst for Efficient Electrochemical CO_2 Reduction. *Adv. Funct. Mater.* **2021**, *31*, 2107072. [CrossRef]

73. He, G.; Yan, M.; Gong, H.; Fei, H.; Wang, S. Ultrafast synthetic strategies under extreme heating conditions toward single-atom catalysts. *Int. J. Extrem. Manuf.* **2022**, *4*, 032003. [CrossRef]

74. Zhang, J.; Zhang, M.; Zeng, Y.; Chen, J.; Qiu, L.; Zhou, H.; Sun, C.; Yu, Y.; Zhu, C.; Zhu, Z.; et al. Single Fe Atom on Hierarchically Porous S, N-Codoped Nanocarbon Derived from Porphyra Enable Boosted Oxygen Catalysis for Rechargeable Zn-Air Batteries. *Small* **2019**, *15*, 1900307. [CrossRef]

75. Jing, H.; Zhao, Z.; Zhang, C.; Liu, W.; Wu, D.; Zhu, C.; Hao, C.; Zhang, J.; Shi, Y. Tuned single atom coordination structures mediated by polarization force and sulfur anions for photovoltaics. *Nano Res.* **2021**, *14*, 4025–4032. [CrossRef]

76. Hu, B.; Huang, A.; Zhang, X.; Chen, Z.; Tu, R.; Zhu, W.; Zhuang, Z.; Chen, C.; Peng, Q.; Li, Y.; et al. Atomic Co/Ni dual sites with N/P-coordination as bifunctional oxygen electrocatalyst for rechargeable zinc-air batteries. *Nano Res.* **2021**, *14*, 3482–3488. [CrossRef]

77. Yuan, K.; Lützenkirchen-Hecht, D.; Li, L.; Shuai, L.; Li, Y.; Cao, R.; Qiu, M.; Zhuang, X.; Leung, M.K.H.; Chen, Y.; et al. Boosting Oxygen Reduction of Single Iron Active Sites via Geometric and Electronic Engineering: Nitrogen and Phosphorus Dual Coordination. *J. Am. Chem. Soc.* **2020**, *142*, 2404–2412. [CrossRef]

78. Li, Z.; Wu, R.; Xiao, S.; Yang, Y.; Lai, L.; Chen, J.S.; Chen, Y. Axial chlorine coordinated iron-nitrogen-carbon single-atom catalysts for efficient electrochemical CO_2 reduction. *Chem. Eng. J.* **2022**, *430*, 132882. [CrossRef]

79. Han, Y.; Wang, Y.; Xu, R.; Chen, W.; Zheng, L.; Han, A.; Zhu, Y.; Zhang, J.; Zhang, H.; Luo, J.; et al. Electronic structure engineering to boost oxygen reduction activity by controlling the coordination of the central metal. *Energy Environ. Sci.* **2018**, *11*, 2348–2352. [CrossRef]

80. Singh, K.P.; Song, M.Y.; Yu, J.S. Iodine-treated heteroatom-doped carbon: Conductivity driven electrocatalytic activity. *J. Mater. Chem. A* **2014**, *2*, 18115–18124. [CrossRef]

81. Wang, N.; Li, X.; Tu, Z.; Zhao, F.; He, J.; Guan, Z.; Huang, C.; Yi, Y.; Li, Y. Synthesis and Electronic Structure of Boron-Graphdiyne with an sp-Hybridized Carbon Skeleton and Its Application in Sodium Storage. *Angew. Chem. Int. Ed.* **2018**, *57*, 3968–3973. [CrossRef]

82. Liu, S.; Jin, M.; Sun, J.; Qin, Y.; Gao, S.; Chen, Y.; Zhang, S.; Luo, J.; Liu, X. Coordination environment engineering to boost electrocatalytic CO_2 reduction performance by introducing boron into single-Fe-atomic catalyst. *Chem. Eng. J.* **2022**, *437*, 135294. [CrossRef]

83. Ni, W.; Gao, Y.; Lin, Y.; Ma, C.; Guo, X.; Wang, S.; Zhang, S. Nonnitrogen Coordination Environment Steering Electrochemical CO_2-to-CO Conversion over Single-Atom Tin Catalysts in a Wide Potential Window. *ACS Catal.* **2021**, *11*, 5212–5221. [CrossRef]

84. Hao, Q.; Zhong, H.X.; Wang, J.Z.; Liu, K.H.; Yan, J.M.; Ren, Z.H.; Zhou, N.; Zhao, X.; Zhang, H.; Liu, D.X.; et al. Nickel dual-atom sites for electrochemical carbon dioxide reduction. *Nat. Synth.* **2022**, *1*, 719–728. [CrossRef]

85. Ding, T.; Liu, X.; Tao, Z.; Liu, T.; Chen, T.; Zhang, W.; Shen, X.; Liu, D.; Wang, S.; Pang, B.; et al. Atomically Precise Dinuclear Site Active toward Electrocatalytic CO_2 Reduction. *J. Am. Chem. Soc.* **2021**, *143*, 11317–11324. [CrossRef]

86. Zhang, N.; Zhang, X.; Kang, Y.; Ye, C.; Jin, R.; Yan, H.; Lin, R.; Yang, J.; Xu, Q.; Wang, Y.; et al. A Supported Pd_2 Dual-Atom Site Catalyst for Efficient Electrochemical CO_2 Reduction. *Angew. Chem. Int. Ed.* **2021**, *60*, 13388–13393. [CrossRef]

87. Wang, Y.; Cheng, W.; Yuan, P.; Yang, G.; Mu, S.; Liang, J.; Xia, H.; Guo, K.; Liu, M.; Zhao, S.; et al. Boosting Nitrogen Reduction to Ammonia on FeN_4 Sites by Atomic Spin Regulation. *Adv. Sci.* **2021**, *8*, 2102915. [CrossRef]

88. Yang, G.G.; Zhu, J.W.; Yuan, P.F.; Hu, Y.F.; Qu, G.; Lu, B.A.; Xue, X.Y.; Yin, H.B.; Cheng, W.Z.; Cheng, J.Q.; et al. Regulating Fe-spin state by atomically dispersed Mn-N in Fe-N-C catalysts with high oxygen reduction activity. *Nat. Commun.* **2021**, *12*, 1734. [CrossRef]

89. Zhang, L.; Si, R.; Liu, H.; Chen, N.; Wang, Q.; Adair, K.; Wang, Z.; Chen, J.; Song, Z.; Li, J.; et al. Atomic layer deposited Pt-Ru dual-metal dimers and identifying their active sites for hydrogen evolution reaction. *Nat. Commun.* **2019**, *10*, 4936. [CrossRef]

90. Xu, W.; Tang, H.; Gu, H.; Xi, H.; Wu, P.; Liang, B.; Liu, Q.; Chen, W. Research progress of asymmetrically coordinated single-atom catalysts for electrocatalytic reactions. *J. Mater. Chem. A* **2022**, *10*, 14732–14746. [CrossRef]

91. Zhang, L.; Jia, Y.; Gao, G.; Yan, X.; Chen, N.; Chen, J.; Soo, M.T.; Wood, B.; Yang, D.; Du, A.; et al. Graphene Defects Trap Atomic Ni Species for Hydrogen and Oxygen Evolution Reactions. *Chem* **2018**, *4*, 285–297. [CrossRef]

92. Liu, J.; Wang, D.; Huang, K.; Dong, J.; Liao, J.; Dai, S.; Tang, X.; Yan, M.; Gong, H.; Liu, J.; et al. Iodine-Doping-Induced Electronic Structure Tuning of Atomic Cobalt for Enhanced Hydrogen Evolution Electrocatalysis. *ACS Nano* **2021**, *15*, 18125–18134. [CrossRef]

93. Zhou, Y.; Song, E.; Chen, W.; Segre, C.U.; Zhou, J.; Lin, Y.-C.; Zhu, C.; Ma, R.; Liu, P.; Chu, S.; et al. Dual-Metal Interbonding as the Chemical Facilitator for Single-Atom Dispersions. *Adv. Mater.* **2020**, *32*, 2003484. [CrossRef]

94. Cui, X.; Gao, L.; Lu, C.H.; Ma, R.; Yang, Y.; Lin, Z. Rational coordination regulation in carbon-based single-metal-atom catalysts for electrocatalytic oxygen reduction reaction. *Nano Converg.* **2022**, *9*, 34. [CrossRef]

95. Sui, R.; Pei, J.; Fang, J.; Zhang, X.; Zhang, Y.; Wei, F.; Chen, W.; Hu, Z.; Hu, S.; Zhu, W.; et al. Engineering Ag–Nx Single-Atom Sites on Porous Concave N-Doped Carbon for Boosting CO_2 Electroreduction. *ACS Appl. Mater. Interfaces* **2021**, *13*, 17736–17744. [CrossRef]

96. Wang, X.; Chen, Z.; Zhao, X.; Yao, T.; Chen, W.; You, R.; Zhao, C.; Wu, G.; Wang, J.; Huang, W.; et al. Regulation of Coordination Number over Single Co Sites: Triggering the Efficient Electroreduction of CO_2. *Angew. Chem.* **2018**, *57*, 1944–1948. [CrossRef]

97. Guo, Y.; Yao, S.; Xue, Y.; Hu, X.; Cui, H.; Zhou, Z. Nickel single-atom catalysts intrinsically promoted by fast pyrolysis for selective electroreduction of CO_2 into CO. *Appl. Catal. B Environ.* **2022**, *304*, 120997. [CrossRef]

98. Lin, L.; Li, H.; Wang, Y.; Li, H.; Wei, P.; Nan, B.; Si, R.; Wang, G.; Bao, X. Temperature-Dependent CO_2 Electroreduction over Fe-N-C and Ni-N-C Single-Atom Catalysts. *Angew. Chem.* **2021**, *60*, 26582–26586. [CrossRef]

99. Ma, W.C.; He, X.Y.; Wang, W.; Xie, S.J.; Zhang, Q.H.; Wang, Y. Electrocatalytic reduction of CO_2 and CO to multi-carbon compounds over Cu-based catalysts. *Chem. Soc. Rev.* **2021**, *50*, 12897–12914. [CrossRef]

100. Guan, A.; Chen, Z.; Quan, Y.; Peng, C.; Wang, Z.; Sham, T.-K.; Yang, C.; Ji, Y.; Qian, L.; Xu, X.; et al. Boosting CO_2 Electroreduction to CH_4 via Tuning Neighboring Single-Copper Sites. *ACS Energy Lett.* **2020**, *5*, 1044–1053. [CrossRef]

101. Feng, J.; Gao, H.; Zheng, L.; Chen, Z.; Zeng, S.; Jiang, C.; Dong, H.; Liu, L.; Zhang, S.; Zhang, X.; et al. A Mn-N$_3$ single-atom catalyst embedded in graphitic carbon nitride for efficient CO_2 electroreduction. *Nat. Commun.* **2020**, *11*, 4341. [CrossRef] [PubMed]

102. Zhao, C.; Dai, X.; Yao, T.; Chen, W.; Wang, X.; Wang, J.; Yang, J.; Wei, S.; Wu, Y.; Li, Y.; et al. Ionic Exchange of Metal–Organic Frameworks to Access Single Nickel Sites for Efficient Electroreduction of CO_2. *J. Am. Chem. Soc.* **2017**, *139*, 8078–8081. [CrossRef] [PubMed]

103. Gong, Y.N.; Jiao, L.; Qian, Y.; Pan, C.Y.; Zheng, L.; Cai, X.; Liu, B.; Yu, S.H.; Jiang, H.L. Regulating the Coordination Environment of MOF-Templated Single-Atom Nickel Electrocatalysts for Boosting CO_2 Reduction. *Angew. Chem.* **2020**, *59*, 2705–2709. [CrossRef] [PubMed]

104. Yang, X.; Cheng, J.; Yang, X.; Xu, Y.; Sun, W.; Liu, N.; Liu, J. Boosting Electrochemical CO_2 Reduction by Controlling Coordination Environment in Atomically Dispersed Ni@N$_x$C$_y$ Catalysts. *ACS Sustain. Chem. Eng.* **2021**, *9*, 6438–6445. [CrossRef]

105. Zhao, X.; Liu, Y. Unveiling the Active Structure of Single Nickel Atom Catalysis: Critical Roles of Charge Capacity and Hydrogen Bonding. *J. Am. Chem. Soc.* **2020**, *142*, 5773–5777. [CrossRef]

106. Zu, X.; Li, X.; Liu, W.; Sun, Y.; Xu, J.; Yao, T.; Yan, W.; Gao, S.; Wang, C.; Wei, S.; et al. Efficient and Robust Carbon Dioxide Electroreduction Enabled by Atomically Dispersed Sn$^{\delta+}$ Sites. *Adv. Mater.* **2019**, *31*, 1808135. [CrossRef]

107. Hou, Y.; Qiu, M.; Kim, M.G.; Liu, P.; Nam, G.; Zhang, T.; Zhuang, X.; Yang, B.; Cho, J.; Chen, M.; et al. Atomically dispersed nickel–nitrogen–sulfur species anchored on porous carbon nanosheets for efficient water oxidation. *Nat. Commun.* **2019**, *10*, 1392. [CrossRef]

108. Wang, Z.; Wang, C.; Hu, Y.; Yang, S.; Yang, J.; Chen, W.; Zhou, H.; Zhou, F.; Wang, L.; Du, J.; et al. Simultaneous diffusion of cation and anion to access N, S co-coordinated Bi-sites for enhanced CO_2 electroreduction. *Nano Res.* **2021**, *14*, 2790–2796. [CrossRef]

109. Jia, C.; Tan, X.; Zhao, Y.; Ren, W.; Li, Y.; Su, Z.; Smith, S.C.; Zhao, C. Sulfur-Dopant-Promoted Electroreduction of CO_2 over Coordinatively Unsaturated Ni-N$_2$ Moieties. *Angew. Chem. Int. Ed.* **2021**, *60*, 23342–23348. [CrossRef]

110. Chen, D.; Zhang, L.H.; Du, J.; Wang, H.; Guo, J.; Zhan, J.; Li, F.; Yu, F. A Tandem Strategy for Enhancing Electrochemical CO_2 Reduction Activity of Single-Atom Cu-S$_1$N$_3$ Catalysts via Integration with Cu Nanoclusters. *Angew. Chem.* **2021**, *60*, 24022–24027. [CrossRef]

111. Chen, S.; Li, X.; Kao, C.-W.; Luo, T.; Chen, K.; Fu, J.; Ma, C.; Li, H.; Li, M.; Chan, T.S.; et al. Unveiling the Proton-Feeding Effect in Sulfur-Doped Fe-N-C Single-Atom Catalyst for Enhanced CO_2 Electroreduction. *Angew. Chem.* **2022**, *61*, e202206233.

112. Gu, X.; Jiao, Y.; Wei, B.; Xu, T.; Zhai, P.; Wei, Y.; Zuo, J.; Liu, W.; Chen, Q.; Yang, Z.; et al. Boron bridged NiN$_4$B$_2$C$_x$ single-atom catalyst for superior electrochemical CO_2 reduction. *Mater. Today* **2022**, *54*, 63–71. [CrossRef]

113. Sun, X.; Tuo, Y.; Ye, C.; Chen, C.; Lu, Q.; Li, G.; Jiang, P.; Chen, S.; Zhu, P.; Ma, M.; et al. Phosphorus Induced Electron Localization of Single Iron Sites for Boosted CO_2 Electroreduction Reaction. *Angew. Chem.* **2021**, *60*, 23614–23618. [CrossRef]

114. Zhang, H.; Li, J.; Xi, S.; Du, Y.; Hai, X.; Wang, J.; Xu, H.; Wu, G.; Zhang, J.; Lu, J.; et al. A Graphene-Supported Single-Atom FeN$_5$ Catalytic Site for Efficient Electrochemical CO_2 Reduction. *Angew. Chem. Int. Ed.* **2019**, *58*, 14871–14876. [CrossRef]

115. Chen, Z.; Huang, A.; Yu, K.; Cui, T.; Zhuang, Z.; Liu, S.; Li, J.; Tu, R.; Sun, K.; Tan, X.; et al. Fe$_1$N$_4$–O$_1$ site with axial Fe–O coordination for highly selective CO_2 reduction over a wide potential range. *Energy Environ. Sci.* **2021**, *14*, 3430–3437. [CrossRef]

116. Wang, X.; Wang, Y.; Sang, X.; Zheng, W.; Zhang, S.; Shuai, L.; Yang, B.; Li, Z.; Chen, J.; Lei, L.; et al. Dynamic Activation of Adsorbed Intermediates via Axial Traction for the Promoted Electrochemical CO_2 Reduction. *Angew. Chem.* **2021**, *60*, 4192–4198. [CrossRef]

117. Huang, M.; Deng, B.; Zhao, X.; Zhang, Z.; Li, F.; Li, K.; Cui, Z.; Kong, L.; Lu, J.; Dong, F.; et al. Template-Sacrificing Synthesis of Well-Defined Asymmetrically Coordinated Single-Atom Catalysts for Highly Efficient CO_2 Electrocatalytic Reduction. *ACS Nano* **2022**, *16*, 2110–2119. [CrossRef]

118. Wu, Y.; Chen, C.; Yan, X.; Sun, X.; Zhu, Q.; Li, P.; Li, Y.; Liu, S.; Ma, J.; Huang, Y.; et al. Boosting CO_2 Electroreduction over a Cadmium Single-Atom Catalyst by Tuning of the Axial Coordination Structure. *Angew. Chem.* **2021**, *133*, 20971–20978. [CrossRef]

119. Huang, J.R.; Qiu, X.F.; Zhao, Z.H.; Zhu, H.L.; Liu, Y.C.; Shi, W.; Liao, P.Q.; Chen, X.M. Single-Product Faradaic Efficiency for Electrocatalytic of CO_2 to CO at Current Density Larger than $1.2\,A\,cm^{-2}$ in Neutral Aqueous Solution by a Single-Atom Nanozyme. *Angew. Chem.* **2022**, *61*, e202210985.

120. Xie, W.; Li, H.; Cui, G.; Li, J.; Song, Y.; Li, S.; Zhang, X.; Lee, J.Y.; Shao, M.; Wei, M. NiSn Atomic Pair on an Integrated Electrode for Synergistic Electrocatalytic CO_2 Reduction. *Angew. Chem.* **2021**, *133*, 7458–7464. [CrossRef]

121. Cao, X.; Zhao, L.; Wulan, B.; Tan, D.; Chen, Q.; Ma, J.; Zhang, J. Atomic Bridging Structure of Nickel—Nitrogen—Carbon for Highly Efficient Electrocatalytic Reduction of CO_2. *Angew. Chem.* **2022**, *61*, e202113918.

122. Li, Y.; Shan, W.; Zachman, M.J.; Wang, M.; Hwang, S.; Tabassum, H.; Yang, J.; Yang, X.; Karakalos, S.; Feng, Z.; et al. Atomically Dispersed Dual-Metal Site Catalysts for Enhanced CO_2 Reduction: Mechanistic Insight into Active Site Structures. *Angew. Chem. Int. Ed.* **2022**, *61*, e202205632.

123. Zhu, J.; Xiao, M.; Ren, D.; Gao, R.; Liu, X.; Zhang, Z.; Luo, D.; Xing, W.; Su, D.; Yu, A.; et al. Quasi-Covalently Coupled Ni–Cu Atomic Pair for Synergistic Electroreduction of CO_2. *J. Am. Chem. Soc.* **2022**, *144*, 9661–9671. [CrossRef] [PubMed]

124. Hao, J.; Zhuang, Z.; Hao, J.; Wang, C.; Lu, S.; Duan, F.; Xu, F.; Du, M.; Zhu, H. Interatomic Electronegativity Offset Dictates Selectivity When Catalyzing the CO_2 Reduction Reaction. *Adv. Energy Mater.* **2022**, *12*, 2200579. [CrossRef]

125. Zeng, Z.; Gan, L.Y.; Bin Yang, H.; Su, X.; Gao, J.; Liu, W.; Matsumoto, H.; Gong, J.; Zhang, J.; Cai, W.; et al. Orbital coupling of hetero-diatomic nickel-iron site for bifunctional electrocatalysis of CO_2 reduction and oxygen evolution. *Nat. Commun.* **2021**, *12*, 4088. [CrossRef]

126. Jiao, L.; Zhu, J.; Zhang, Y.; Yang, W.; Zhou, S.; Li, A.; Xie, C.; Zheng, X.; Zhou, W.; Yu, S.-H.; et al. Non-Bonding Interaction of Neighboring Fe and Ni Single-Atom Pairs on MOF-Derived N-Doped Carbon for Enhanced CO_2 Electroreduction. *J. Am. Chem. Soc.* **2021**, *143*, 19417–19424. [CrossRef]

127. Ren, W.; Tan, X.; Yang, W.; Jia, C.; Xu, S.; Wang, K.; Smith, S.C.; Zhao, C. Isolated Diatomic Ni-Fe Metal–Nitrogen Sites for Synergistic Electroreduction of CO_2. *Angew. Chem.* **2019**, *58*, 6972–6976. [CrossRef]

128. Cheng, H.; Wu, X.; Feng, M.; Li, X.; Lei, G.; Fan, Z.; Pan, D.; Cui, F.; He, G. Atomically Dispersed Ni/Cu Dual Sites for Boosting the CO_2 Reduction Reaction. *ACS Catal.* **2021**, *11*, 12673–12681. [CrossRef]

129. Yi, J.D.; Gao, X.; Zhou, H.; Chen, W.; Wu, Y. Design of Co-Cu Diatomic Site Catalysts for High-efficiency Synergistic CO_2 Electroreduction at Industrial-level Current Density. *Angew. Chem.* **2022**, *61*, e202212329. [CrossRef]

130. Li, Y.; Wei, B.; Zhu, M.; Chen, J.; Jiang, Q.; Yang, B.; Hou, Y.; Lei, L.; Li, Z.; Zhang, R.; et al. Synergistic Effect of Atomically Dispersed Ni–Zn Pair Sites for Enhanced CO_2 Electroreduction. *Adv. Mater.* **2021**, *33*, 2102212. [CrossRef]

131. Zhu, W.; Zhang, L.; Liu, S.; Li, A.; Yuan, X.; Hu, C.; Zhang, G.; Deng, W.; Zang, K.; Luo, J.; et al. Enhanced CO_2 Electroreduction on Neighboring Zn/Co Monomers by Electronic Effect. *Angew. Chem.* **2020**, *59*, 12664–12668. [CrossRef]

132. Qiu, X.F.; Huang, J.R.; Yu, C.; Zhao, Z.H.; Zhu, H.L.; Ke, Z.; Liao, P.Q.; Chen, X.M. A Stable and Conductive Covalent Organic Framework with Isolated Active Sites for Highly Selective Electroreduction of Carbon Dioxide to Acetate. *Angew. Chem.* **2022**, *61*, e202206470.

133. Shao, P.; Zhou, W.; Hong, Q.L.; Yi, L.; Zheng, L.; Wang, W.; Zhang, H.X.; Zhang, H.; Zhang, J. Synthesis of a Boron–Imidazolate Framework Nanosheet with Dimer Copper Units for CO_2 Electroreduction to Ethylene. *Angew. Chem.* **2021**, *60*, 16687–16692. [CrossRef]

134. Zhu, H.L.; Chen, H.Y.; Han, Y.X.; Zhao, Z.H.; Liao, P.Q.; Chen, X.M. A Porous π–π Stacking Framework with Dicopper (I) Sites and Adjacent Proton Relays for Electroreduction of CO_2 to C_{2+} Products. *J. Am. Chem. Soc.* **2022**, *144*, 13319–13326. [CrossRef]

135. Lin, L.; Li, H.; Yan, C.; Li, H.; Si, R.; Li, M.; Xiao, J.; Wang, G.; Bao, X. Synergistic Catalysis over Iron-Nitrogen Sites Anchored with Cobalt Phthalocyanine for Efficient CO_2 Electroreduction. *Adv. Mater.* **2019**, *31*, 1903470. [CrossRef]

136. Pan, Y.; Lin, R.; Chen, Y.; Liu, S.; Zhu, W.; Cao, X.; Chen, W.; Wu, K.; Cheong, W.-C.; Wang, Y.; et al. Design of Single-Atom Co–N_5 Catalytic Site: A Robust Electrocatalyst for CO_2 Reduction with Nearly 100% CO Selectivity and Remarkable Stability. *J. Am. Chem. Soc.* **2018**, *140*, 4218–4221. [CrossRef]

137. Wang, J.; Huang, X.; Xi, S.; Lee, J.M.; Wang, C.; Du, Y.; Wang, X. Linkage Effect in the Heterogenization of Cobalt Complexes by Doped Graphene for Electrocatalytic CO_2 Reduction. *Angew. Chem.* **2019**, *58*, 13532–13539. [CrossRef]

138. Jiao, J.; Lin, R.; Liu, S.; Cheong, W.-C.; Zhang, C.; Chen, Z.; Pan, Y.; Tang, J.; Wu, K.; Hung, S.-F.; et al. Copper atom-pair catalyst anchored on alloy nanowires for selective and efficient electrochemical reduction of CO_2. *Nat. Chem.* **2019**, *11*, 222–228. [CrossRef]

139. Han, L.L.; Liu, X.J.; He, J.; Liang, Z.X.; Wang, H.T.; Bak, S.M.; Zhang, J.M.; Hunt, A.; Waluyo, I.; Pong, W.F.; et al. Modification of the Coordination Environment of Active Sites on MoC for High-Efficiency CH_4 Production. *Adv. Energy Mater.* **2021**, *11*, 2100044. [CrossRef]

140. Chen, Y.; Qiao, S.; Tang, Y.; Du, Y.; Zhang, D.; Wang, W.; Xie, H.; Liu, C. Precise and scalable fabrication of metal pair-site catalysts enabled by intramolecular integrated donor atoms. *J. Mater. Chem. A* **2022**, *10*, 25307–25318. [CrossRef]

141. Wei, T.; Bao, H.; Wang, X.; Zhang, S.; Liu, Q.; Luo, J.; Liu, X. Ionic Liquid-assisted electrocatalytic NO reduction to NH_3 by P-doped MoS_2. *ChemCatChem* **2023**, e202201411. [CrossRef]

142. Zhang, L.H.; Han, L.L.; Liu, H.X.; Liu, X.J.; Luo, J. Potential-Cycling Synthesis of Single Platinum Atoms for Efficient Hydrogen Evolution in Neutral Media. *Angew. Chem.* **2017**, *56*, 13694–13698. [CrossRef] [PubMed]

143. He, X.; Zhang, H.; Zhang, X.; Zhang, Y.; He, Q.; Chen, H.; Cheng, Y.; Peng, M.; Qin, X.; Ji, H.; et al. Building up libraries and production line for single atom catalysts with precursor-atomization strategy. *Nat. Commun.* **2022**, *13*, 5721. [CrossRef] [PubMed]

144. Wei, T.; Zhang, S.; Liu, Q.; Qiu, Y.; Luo, J.; Liu, X. Oxygen Vacancy-Rich Amorphous Copper Oxide Enables Highly Selective Electroreduction of Carbon Dioxide to Ethylene. *Acta Phys. Chim. Sin.* **2023**, *39*, 202207026. [CrossRef]

145. Bo, L.; Zhen, L.; Xin, W.; Zonglong, Z. Interface functionalization in inverted perovskite solar cells: From material perspective. *Nano Res. Energy* **2022**, *1*, e9120011.

146. Ahui, H.; Xin, W.; Xiaofang, L.; Ronghai, Y.; Jianglan, S. Inorganic microporous membranes for hydrogen separation: Challenges and solutions. *Nano Res. Energy* **2022**, *1*, e9120013.

147. Li, J.; Chen, G.; Zhu, Y.; Liang, Z.; Pei, A.; Wu, C.-L.; Wang, H.; Lee, H.R.; Liu, K.; Chu, S.; et al. Efficient electrocatalytic CO_2 reduction on a three-phase interface. *Nat. Catal.* **2018**, *1*, 592–600. [CrossRef]

148. Gao, S.S.; Liu, Y.F.; Xie, Z.Y.; Qiu, Y.; Zhuo, L.C.; Qin, Y.J.; Ren, J.Q.; Zhang, S.S.; Hu, G.Z.; Luo, J.; et al. Metal-Free Bifunctional Ordered Mesoporous Carbon for Reversible $Zn-CO_2$ Batteries. *Small Methods* **2021**, *5*, 2001039. [CrossRef]

149. Wei, T.; Liu, W.; Zhang, S.; Liu, Q.; Luo, J.; Liu, X. A dual-functional Bi-doped Co_3O_4 nanosheet array towards high efficiency 5-hydroxymethylfurfural oxidation and hydrogen production. *Chem. Commun.* **2023**, *59*, 442–445. [CrossRef]

150. Lv, F.; Han, N.; Qiu, Y.; Liu, X.J.; Luo, J.; Li, Y.G. Transition metal macrocycles for heterogeneous electrochemical CO_2 reduction. *Coord. Chem. Rev.* **2020**, *422*, 213435. [CrossRef]

151. Wang, K.; Wu, Y.; Cao, X.; Gu, L.; Hu, J. A $Zn–CO_2$ Flow Battery Generating Electricity and Methane. *Adv. Funct. Mater.* **2020**, *30*, 1908965. [CrossRef]

152. Wang, X.Z.; Liu, S.; Zhang, H.; Zhang, S.S.; Meng, G.; Liu, Q.; Sun, Z.Y.; Luo, J.; Liu, X.J. Polycrystalline SnS_x nanofilm enables CO_2 electroreduction to formate with high current density. *Chem. Commun.* **2022**, *58*, 7654–7657. [CrossRef]

153. Leverett, J.; Daiyan, R.; Gong, L.L.; Iputera, K.; Tong, Z.Z.; Qu, J.T.; Ma, Z.P.; Zhang, Q.R.; Cheong, S.S.; Cairney, J.; et al. Designing Undercoordinated Ni-N-x and Fe-N-x on Holey Graphene for Electrochemical CO_2 Conversion to Syngas. *ACS Nano* **2021**, *15*, 12006–12018. [CrossRef]

154. Zou, X.Y.; Ma, C.; Li, A.; Gao, Z.; Shadike, Z.; Jiang, K.; Zhang, J.L.; Huang, Z.; Zhu, L. Nanoparticle-Assisted Ni-Co Binary Single-Atom Catalysts Supported on Carbon Nanotubes for Efficient Electroreduction of CO_2 to Syngas with Controllable CO/H_2 Ratios. *ACS Appl. Energy Mater.* **2021**, *4*, 9572–9581. [CrossRef]

155. Cheng, M.J.; Clark, E.; Pham, H.; Bell, A.; Head-Gordon, M. Quantum mechanical screening of single-atom bimetallic alloys for the selective reduction of CO_2 to C_1 hydrocarbons. *ACS Catal.* **2016**, *6*, 7769–7777. [CrossRef]

156. Zhao, J.; Zhao, J.X.; Li, F.Y.; Chen, Z.F. Copper Dimer Supported on a C_2N Layer as an Efficient Electrocatalyst for CO_2 Reduction Reaction: A Computational Study. *J. Phys. Chem. C* **2018**, *122*, 19712–19721. [CrossRef]

157. Danye, L.; Qing, Z.; Chaoquan, H.; Dong, C.; Hui, L.; Yongsheng, H.; Lin, X.; Qingbo, Z.; Jun, Y. Light doping of tungsten into copper-platinum nanoalloys for boosting their electrocatalytic performance in methanol oxidation. *Nano Res. Energy* **2022**, *1*, e9120017.

158. Lin, L.; Liu, T.; Xiao, J.; Li, H.; Wei, P.; Gao, D.; Nan, B.; Si, R.; Wang, G.; Bao, X.; et al. Enhancing CO_2 Electroreduction to Methane with a Cobalt Phthalocyanine and Zinc–Nitrogen–Carbon Tandem Catalyst. *Angew. Chem.* **2020**, *59*, 22408–22413. [CrossRef]

159. Zengxia, P. Symmetric is nonidentical: Operation history matters for Zn metal anode. *Nano Res. Energy* **2022**, *1*, e9120023.

160. Wang, X.; Huang, G.; Pan, Z.; Kang, S.; Ma, S.; Shen, P.K.; Zhu, J. One-pot synthesis of $Mn_2P-Mn_2O_3$ heterogeneous nanoparticles in a P, N -doped three-dimensional porous carbon framework as a highly efficient bifunctional electrocatalyst for overall water splitting. *Chem. Eng. J.* **2022**, *428*, 131190. [CrossRef]

161. Ju, W.; Bagger, A.; Hao, G.P.; Varela, A.S.; Sinev, I.; Bon, V.; Roldan Cuenya, B.; Kaskel, S.; Rossmeisl, J.; Strasser, P.; et al. Understanding activity and selectivity of metal-nitrogen-doped carbon catalysts for electrochemical reduction of CO_2. *Nat. Commun.* **2017**, *8*, 944. [CrossRef] [PubMed]

162. Zhu, J.; Jiang, E.; Wang, X.; Pan, Z.; Xu, X.; Ma, S.; Kang Shen, P.; Pan, L.; Eguchi, M.; Nanjundan, A.K.; et al. Gram-Scale production of Cu_3P-Cu_2O Janus nanoparticles into nitrogen and phosphorous doped porous carbon framework as bifunctional electrocatalysts for overall water splitting. *Chem. Eng. J.* **2022**, *427*, 130946. [CrossRef]

163. Zhang, B.; Zhang, Y.; Hou, M.; Wang, W.; Hu, S.; Cen, W.; Cao, X.; Qiao, S.; Han, B.H. Pristine, metal ion and metal cluster modified conjugated triazine frameworks as electrocatalysts for hydrogen evolution reaction. *J. Mater. Chem. A* **2021**, *9*, 10146–10159. [CrossRef]

164. Feng, Y.; Li, Z.; Li, S.; Yang, M.; Ma, R.; Wang, J. One stone two birds: Vanadium doping as dual roles in self-reduced Pt clusters and accelerated water splitting. *J. Energy Chem.* **2022**, *66*, 493–501. [CrossRef]

165. Zhang, H.; Qiu, Y.; Zhang, S.S.; Liu, Q.; Luo, J.; Liu, X.J. Nitrogen-incorporated iron phosphosulfide nanosheets as efficient bifunctional electrocatalysts for energy-saving hydrogen evolution. *Ionics* **2022**, *28*, 3927–3934. [CrossRef]

166. Chen, W.; Li, X.; Wei, X.; Liao, G.; Wang, J.; Li, L. Activation of peroxymonosulfate for degrading ibuprofen via single atom Cu anchored by carbon skeleton and chlorine atom: The radical and non-radical pathways. *Sci. Total Environ.* **2023**, *858*, 160097. [CrossRef]

167. Li, Y.; Zeng, Y.; Chen, Y.; Luan, D.; Gao, S.; Lou, X.W. Mesoporous N-rich Carbon with Single-Ni Atoms as a Multifunctional Sulfur Host for Li-S Batteries. *Angew. Chem.* **2022**, *61*, e202212680.

168. Liu, W.; Feng, J.; Wei, T.; Liu, Q.; Zhang, S.; Luo, Y.; Luo, J.; Liu, X. Active-site and interface engineering of cathode materials for aqueous Zn-Gas batteries. *Nano Res.* **2022**, 1–22. [CrossRef]

169. Arandia, A.; Yim, J.; Warraich, H.; Leppakangas, E.; Bes, R.; Lempelto, A.; Gell, L.; Jiang, H.; Meinander, K.; Viinikainen, T.; et al. Effect of atomic layer deposited zinc promoter on the activity of copper-on-zirconia catalysts in the hydrogenation of carbon dioxide to methanol. *Appl. Catal. B Environ.* **2023**, *321*, 122046. [CrossRef]

170. Schmelz, D.; Gerold, K.; Kasebier, T.; Sergeev, N.; Szeghalmi, A.; Zeitner, U.D. Optical properties of black silicon structures ALD-coated with Al_2O_3. *Nanotechnology* **2023**, *34*, 015704. [CrossRef]

171. Zhang, H.; Luo, Y.; Chu, P.; Liu, Q.; Liu, X.; Zhang, S.; Luo, J.; Wang, X.; Hu, G. Recent advances in non-noble metal-based bifunctional electrocatalysts for overall seawater splitting. *J. Alloys Compd.* **2022**, *922*, 166113. [CrossRef]

172. Zhang, C.X.; Liu, H.X.; Liu, Y.F.; Liu, X.J.; Mi, Y.Y.; Guo, R.J.; Sun, J.Q.; Bao, H.H.; He, J.; Qiu, Y.; et al. Rh_2S_3/N-Doped Carbon Hybrids as pH-Universal Bifunctional Electrocatalysts for Energy-Saving Hydrogen Evolution. *Small Methods* **2020**, *4*, 2000208. [CrossRef]

173. Eid, K.; Sliem, M.H.; Al-Ejji, M.; Abdullah, A.M.; Harfouche, M.; Varma, R.S. Hierarchical Porous Carbon Nitride-Crumpled Nanosheet-Embedded Copper Single Atoms: An Efficient Catalyst for Carbon Monoxide Oxidation. *ACS Appl. Mater. Interfaces* **2022**, *14*, 40749–40760. [CrossRef]

174. Cheng, Y.; Song, H.; Yu, J.; Chang, J.; Waterhouse, G.I.N.; Tang, Z.; Yang, B.; Lu, S. Carbon dots-derived carbon nanoflowers decorated with cobalt single atoms and nanoparticles as efficient electrocatalysts for oxygen reduction. *Chin. J. Catal.* **2022**, *43*, 2443–2452. [CrossRef]

175. Xu, J.; Zhang, C.X.; Liu, H.X.; Sun, J.Q.; Xie, R.C.; Qiu, Y.; Lu, F.; Liu, Y.F.; Zhuo, L.C.; Liu, X.J.; et al. Amorphous MoO_X-Stabilized single platinum atoms with ultrahigh mass activity for acidic hydrogen evolution. *Nano Energy* **2020**, *70*, 104529. [CrossRef]

176. Liu, Y.; Fan, X.; Bian, W.; Yang, Y.; Huang, P.; Hofer, W.A.; Huang, H.; Lin, H.; Li, Y.; Lee, S.T.; et al. High-loading Fe1 sites on vanadium disulfides: A scalable and non-defect-stabilized single atom catalyst for electrochemical nitrogen reduction. *J. Mater. Chem. A* **2022**, *10*, 21142–21148. [CrossRef]

177. Yao, Y.; Zhao, L.; Dai, J.; Wang, J.; Fang, C.; Zhan, G.; Zheng, Q.; Hou, W.; Zhang, L. Single Atom Ru Monolithic Electrode for Efficient Chlorine Evolution and Nitrate Reduction. *Angew. Chem.* **2022**, *61*, e202208215. [CrossRef]

178. Peng, X.Y.; Mi, Y.Y.; Liu, X.J.; Sun, J.Q.; Qiu, Y.; Zhang, S.S.; Ke, X.X.; Wang, X.Z.; Luo, J. Self-driven dual hydrogen production system based on a bifunctional single-atomic Rh catalyst. *J. Mater. Chem. A* **2022**, *10*, 6134–6145. [CrossRef]

179. Liu, H.; Hu, Z.; Liu, Q.; Sun, P.; Wang, Y.; Chou, S.; Hu, Z.; Zhang, Z. Single-atom Ru anchored in nitrogen-doped MXene ($Ti_3C_2T_x$) as an efficient catalyst for the hydrogen evolution reaction at all pH values. *J. Mater. Chem. A* **2020**, *8*, 24710–24717. [CrossRef]

180. Xue, Y.; Huang, B.; Yi, Y.; Guo, Y.; Zuo, Z.; Li, Y.; Jia, Z.; Liu, H.; Li, Y. Anchoring zero valence single atoms of nickel and iron on graphdiyne for hydrogen evolution. *Nat. Commun.* **2018**, *9*, 1460. [CrossRef]

181. Peng, X.Y.; Hou, J.R.; Mi, Y.Y.; Sun, J.Q.; Qi, G.C.; Qin, Y.J.; Zhang, S.S.; Qiu, Y.; Luo, J.; Liu, X.J.; et al. Bifunctional single-atomic Mn sites for energy-efficient hydrogen production. *Nanoscale* **2021**, *13*, 4767–4773. [CrossRef] [PubMed]

182. Qi, D.F.; Liu, S.; Chen, H.H.; Lai, S.H.; Qin, Y.J.; Qiu, Y.; Dai, S.; Zhang, S.S.; Luo, J.; Liu, X.J. Rh nanoparticle functionalized heteroatom-doped hollow carbon spheres for efficient electrocatalytic hydrogen evolution. *Mater. Chem. Front.* **2021**, *5*, 3125–3131. [CrossRef]

183. Zou, L.; Wei, Y.S.; Hou, C.C.; Li, C.; Xu, Q. Single-Atom Catalysts Derived from Metal-Organic Frameworks for Electrochemical Applications. *Small* **2021**, *17*, e2004809. [CrossRef] [PubMed]

184. Xu, H.; Rebollar, D.; He, H.; Chong, L.; Liu, Y.; Liu, C.; Sun, C.-J.; Li, T.; Muntean, J.V.; Winans, R.E.; et al. Highly selective electrocatalytic CO_2 reduction to ethanol by metallic clusters dynamically formed from atomically dispersed copper. *Nat. Energy* **2020**, *5*, 623–632. [CrossRef]

185. Peng, X.N.; Bao, H.H.; Sun, J.Q.; Mao, Z.Y.; Qiu, Y.; Mo, Z.J.; Zhuo, L.C.; Zhang, S.S.; Luo, J.; Liu, X.J.; et al. Heteroatom coordination induces electric field polarization of single Pt sites to promote hydrogen evolution activity. *Nanoscale* **2021**, *13*, 7134–7139. [CrossRef]

186. Zhao, L.; Wang, S.Q.; Liang, S.; An, Q.; Fu, J.; Hu, J.S. Coordination anchoring synthesis of high-density single-metal-atom sites for electrocatalysis. *Coord. Chem. Rev.* **2022**, *466*, 214603. [CrossRef]

187. Zhang, H.; Liu, W.; Cao, D.; Cheng, D. Carbon-based material-supported single-atom catalysts for energy conversion. *iScience* **2022**, *25*, 104367. [CrossRef]

188. Liu, X.J.; Xi, W.; Li, C.; Li, X.B.; Shi, J.; Shen, Y.L.; He, J.; Zhang, L.H.; Xie, L.; Sun, X.M.; et al. Nanoporous Zn-doped Co_3O_4 sheets with single-unit-cell-wide lateral surfaces for efficient oxygen evolution and water splitting. *Nano Energy* **2018**, *44*, 371–377. [CrossRef]

189. Liu, X.J.; He, J.; Zhao, S.Z.; Liu, Y.P.; Zhao, Z.; Luo, J.; Hu, G.Z.; Sun, X.M.; Ding, Y. Self-powered H_2 production with bifunctional hydrazine as sole consumable. *Nat. Commun.* **2018**, *9*, 4365. [CrossRef]

190. Zhang, F.; Zhu, Y.; Lin, Q.; Zhang, L.; Zhang, X.; Wang, H. Noble-metal single-atoms in thermocatalysis, electrocatalysis, and photocatalysis. *Energy Environ. Sci.* **2021**, *14*, 2954–3009. [CrossRef]

191. Han, L.; Ren, Z.; Ou, P.; Cheng, H.; Rui, N.; Lin, L.; Liu, X.; Zhuo, L.; Song, J.; Sun, J.; et al. Modulating Single-Atom Palladium Sites with Copper for Enhanced Ambient Ammonia Electrosynthesis. *Angew. Chem.* **2021**, *60*, 345–350. [CrossRef]

192. Zeng, X.; Tu, Z.; Yuan, Y.; Liao, L.; Xiao, C.; Wen, Y.; Xiong, K. Two-Dimensional Transition Metal-Hexaaminobenzene Monolayer Single-Atom Catalyst for Electrocatalytic Carbon Dioxide Reduction. *Nanomaterials* **2022**, *12*, 4005. [CrossRef]

193. Meng, G.; Wei, T.; Liu, W.; Li, W.; Zhang, S.; Liu, W.; Liu, Q.; Bao, H.; Luo, J.; Liu, X.; et al. NiFe layered double hydroxide nanosheet array for high-efficiency electrocatalytic reduction of nitric oxide to ammonia. *Chem. Commun.* **2022**, *58*, 8097–8100. [CrossRef]

194. Gao, S.; Wei, T.; Sun, J.; Liu, Q.; Ma, D.; Liu, W.; Zhang, S.; Luo, J.; Liu, X. Atomically Dispersed Metal-Based Catalysts for Zn–CO_2 Batteries. *Small Struct.* **2022**, *3*, 2200086. [CrossRef]

195. Zhong, M.; Tran, K.; Min, Y.; Wang, C.; Wang, Z.; Dinh, C.-T.; De Luna, P.; Yu, Z.; Rasouli, A.S.; Brodersen, P.; et al. Accelerated discovery of CO_2 electrocatalysts using active machine learning. *Nature* **2020**, *581*, 178–183. [CrossRef]

196. Liu, H.X.; Liu, X.J.; Mao, Z.Y.; Zhao, Z.; Peng, X.Y.; Luo, J.; Sun, X.M. Plasma-activated $Co_3(PO_4)_2$ nanosheet arrays with Co^{3+}-Rich surfaces for overall water water splitting. *J. Power Sources* **2018**, *400*, 190–197. [CrossRef]

197. Li, Y.; Zhang, L.H.; Liu, R.R.; Cao, Z.; Sun, X.M.; Liu, X.J.; Luo, J. WO_3@alpha-Fe_2O_3 Heterojunction Arrays with Improved Photoelectrochemical Behavior for Neutral pH Water Splitting. *ChemCatChem* **2016**, *8*, 2765–2770. [CrossRef]

198. Li, P.S.; Wang, S.Y.; Samo, I.A.; Zhang, X.H.; Wang, Z.L.; Wang, C.; Li, Y.; Du, Y.Y.; Zhong, Y.; Cheng, C.T.; et al. Common-Ion Effect Triggered Highly Sustained Seawater Electrolysis with Additional NaCl Production. *Research* **2020**, *2020*, 2872141. [CrossRef]

199. Jiang, E.; Li, J.; Li, X.; Ali, A.; Wang, G.; Ma, S.; Kang Shen, P.; Zhu, J. MoP-Mo_2C quantum dot heterostructures uniformly hosted on a heteroatom-doped 3D porous carbon sheet network as an efficient bifunctional electrocatalyst for overall water splitting. *Chem. Eng. J.* **2022**, *431*, 133719. [CrossRef]

200. Huang, W.; Zhou, D.J.; Qi, G.C.; Liu, X.J. Fe-doped MoS_2 nanosheets array for high-current-density seawater electrolysis. *Nanotechnology* **2021**, *32*, 415403. [CrossRef]

201. Liu, H.; Liu, Y.; Li, M.; Liu, X.; Luo, J. Transition-metal-based electrocatalysts for hydrazine-assisted hydrogen production. *Mater. Today Adv.* **2020**, *7*, 100083. [CrossRef]

202. Wang, M.; Zhang, H.; Liu, Y.; Pan, Y. Research progress of precise structural regulation of single atom catalyst for accelerating electrocatalytic oxygen reduction reaction. *J. Energy Chem.* **2022**, *72*, 56–72. [CrossRef]

203. Liu, H.X.; Peng, X.Y.; Liu, X.J.; Qi, G.C.; Luo, J. Porous Mn-Doped FeP/$Co_3(PO_4)_2$ Nanosheets as Efficient Electrocatalysts for Overall Water Splitting in a Wide pH Range. *ChemSusChem* **2019**, *12*, 1334–1341. [CrossRef] [PubMed]

204. Wang, H.; Zhang, F.; Jin, M.; Zhao, D.; Fan, X.; Li, Z.; Luo, Y.; Zheng, D.; Li, T.; Wang, Y.; et al. V-doped TiO_2 nanobelt array for high-efficiency electrocatalytic nitrite reduction to ammonia. *Mater. Today Phys.* **2023**, *30*, 100944. [CrossRef]

205. Wang, J.; Xu, R.; Li, Y.; Li, Y.; Yang, M.; Yang, G.; Zhao, Y.; Gao, F. Recent progress, developing strategies, theoretical insights, and perspectives towards high-performance copper single atom electrocatalysts. *Mater. Today Energy* **2021**, *21*, 100761. [CrossRef]

206. Yang, M.; Sun, J.; Qin, Y.; Yang, H.; Zhang, S.; Liu, X.; Luo, J. Hollow CoFe-layered double hydroxide polyhedrons for highly efficient CO_2 electrolysis. *Sci. China Mater.* **2022**, *65*, 536–542. [CrossRef]

207. Anuratha, K.S.; Rinawati, M.; Wu, T.H.; Yeh, M.H.; Lin, J.Y. Recent Development of Nickel-Based Electrocatalysts for Urea Electrolysis in Alkaline Solution. *Nanomaterials* **2022**, *12*, 2970. [CrossRef]